Volume 17
Number 2

December *2015*
(ISSN 1109-1606)

Journal of APPLIED ELECTROMAGNETISM

JAE

Institute of Communication and Computer Systems

Athens - GREECE

Volume 17 December 2015
Number 2 (ISSN 1109-1606)

JOURNAL
OF
APPLIED ELECTROMAGNETISM

Trans Black Sea Region Union of Applied Electromagnetism

BSUAE

Institute of Communication and Computer Systems

Athens - GREECE

Volume 17 **Number 2**

December 2015

TRANS BLACK SEA REGION UNION OF APPLIED ELECTROMAGNETISM (BSUAE)

JOURNAL OF APPLIED ELECTROMAGNETISM

Institute of Communication and Computer Systems

Athens - GREECE

Editor: Panayiotis Frangos (Greece), pfrangos@central.ntua.gr

Honorary Editor: Nikolaos K. Uzunoglu (Greece), nuzu@central.ntua.gr

Board of Associate Editors

D. Dimitrov (Bulgaria), dcd@tu-sofia.bg
V. Dumbrava (Lithuania), vydum@ktu.lt
G. Georgiev (Bulgaria), gngeorgiev@yahoo.com
G. Matsopoulos (Greece), gmatso@esd.ece.ntua.gr

Editorial Board

ALBANIA
G. Bardhyf, bardhylgolemi@live.com
C. Pirro, p_cipo@yahoo.com

ARMENIA
H. Bagdasarian, hovik@seua.sci.am
H. Terzian, hterzian@seua.sci.am

BULGARIA
A. Antonov, asantonov@abv.bg
A. Lazarov, lazarov@bfu.bg
S. Savov, savovsv@yahoo.com

GEORGIA
R. Zaridze, rzaridze@laetsu.org

GERMANY
M. Georgieva – Grosse, mngeorgieva@yahoo.de

GREECE
H. Anastassiu, ANASTASIOU.Christos@haicorp.com
I. Avramopoulos, hav@mail.ntua.gr
G. Fikioris, gfiki@cc.ece.ntua.gr
J. Kanellopoulos, ikanell@cc.ece.ntua.gr
G. Karagiannidis, geokarag@auth.gr
G. Kliros, gsksma@hol.gr
T. Mathiopoulos, mathio@space.noa.gr
C. Moschovitis, harism@noc.ntua.gr
K. Nikita, knikita@cc.ece.ntua.gr
I. Ouranos, iouranos@central.ntua.gr
E. Papkelis, spapkel@central.ntua.gr
J. Sahalos, sahalos@auth.gr
M. Theologou, theolog@cs.ntua.gr

N. Triantafyllou, nitriant@central.ntua.gr
K. Ksystra, katksy@central.ntua.gr
A. Malamou, annamalamou@yahoo.gr

JORDAN
N. Dib, nihad@just.edu.jo

KAZAKSHTAN
S. Sautbekov, sautbek@mail.ru

LITHUANIA
L. Svilainis, linas.svilainis@ktu.lt

RUSSIA
M. Bakunov, bakunov@rf.unn.runnet.ru
A. Grigoriev, adgrigoriev@mail.ru

SERBIA
B. Reljin, ereljin@ubbg.etf.bg.ac.yu

SPAIN
E. Gago – Ribas, egr@tsc.uniovi.es
M. Gonzalez – Morales, gonmor@yllera.tel.uva.es

UNITED KINGDOM
G. Goussetis, G.Goussetis@hw.ac.uk

Publishing Department

M. Georgieva – Grosse, mngeorgieva @yahoo.de
N. Triantafyllou, nitriant@central.ntua.gr
K. Ksystra, katksy@central.ntua.gr
A. Malamou, annamalamou@yahoo.gr

Journal of Applied Electromagnetism

Copyright Form

The undersigned I confirm that I agree the publication of the article

in the Journal of Applied Electromagnetism and the copyright to belong to Trans Black Sea Union of Applied Electromagnetism. I understand that I have the full right to reuse this manuscript for my own purposes.

Name:

Surname:

Address:

E-mail:

Signed:

***Please send the previous form signed either by e-mail to pfrangos@central.ntua.gr , or by fax to the fax number: +30 210 772 2281, attention of Prof. P. Frangos.**

Address

Institute of Communication and Computer Systems

National Technical University of Athens

9, Iroon Polytechniou str.

15773 Athens - GREECE

Tel: (+30) 2107723694

Fax: (+30) 2107722281, attention of Prof. P. Frangos

e-mail: pfrangos@central.ntua.gr

Web site: **http://jae.ece.ntua.gr**

TRANS BLACK SEA REGION UNION OF APPLIED ELECTROMAGNETISM (BSUAE)

JOURNAL OF APPLIED ELECTROMAGNETISM (JAE)

Volume 17 Number 2 December 2015

CONTENTS

PLANE WAVE DIFFRACTION BY THE MULTILAYER STRUCTURE OF THE INFINITE 2D PERIODIC LATTICES

I. M. Petoev, V. A. Tabatadze, D. G. Kakulia and R. S. Zaridze 1

Plane electromagnetic wave diffraction problem on the multilayer structure of the infinite 2D periodic lattices is studied. The main goal of this investigation is to find the system parameters, for which it has the metamaterial properties - as the result of multiple resonances. The lattice element represents the conductor wire with small electric radius. There are considered the cases when this structure is embedded inside of the dielectric layer and also in the free space. For the first case the Method of Auxiliary Sources (MAS) is used. Interaction between several resonant layers amplifies metamaterial properties.

HOMOMORPHIC FILTERING APPROACH FOR NARROW BAND IMAGES ENHANCEMENT

V. M. Georgieva 13

The application of narrow band imaging (NBI) in endoscopy improves the accuracy in diagnosis, including reduction in cost and time. It allows better definition between the epithelial surface and the adjacent vascular net via the application of narrow-bandwidth filters to standard white-light endoscopy. The fact, that only selected bandwidths are emitted results in a lower brightness, which requires special high –sensitive dual mode CCDs.

In the paper is presented an approach for NB images enhancement using improved homomorphic filtering. Traditional homomorphic filtering is based on Fourier transform, which has higher resolution in frequency domain and lower resolution in spatial domain. The proposed algorithm includes homomorphic filtering based on wavelet packet transform as first step of improving, and contrast limited adaptive histogram equalization (CLAHE) as the second improving step to adjust its whole luminousness. An adaptive threshold estimation method for image denoising in the wavelet domain is used, for modeling of detail sub-band coefficients. An effective algorithm was treatment by optimization of some parameters of the CLAHE and wavelet transformation on the base of objective quantitative estimation parameters. The main goal is noise reduction and improving the quality of the diagnostic images.

Some results of the experiments with colonoscopy images are presented, which were made by computer simulation in MATLAB environment.

IEEE 802.11AC STANDARD IMPACT ON TRANSMISSION OF VOIP SERVICE

A. Matusevičius, T. Adomkus, L. Narbutaite and R. Bruzgiene **23**

In our days practically all users want to have a connection to a wireless network not only at home, but in any place at any time. So, the users want that their network devices as much as possible be mobile and at the same time ensure high Quality of Services (QoS). Local wireless networks (WiFi) are good choice for the users' mobility, however it have a number of disadvantages, as the limited network's bandwidth and the pollution of the radio ether. That is the reason for 5 GHz frequency use as it is clearer comparing with 2.4 GHz frequency range. More flexible and more adaptable wireless networks, based on a 5 GHz frequency range are IEEE802.11n (5GHz) and IEEE 802.11ac. The wireless networks over 5 GHz frequency range are more advanced due to the more clear radio ether and improved network's bandwidth. According to this, the authors compared 802.11ac with 802.11n (5GHz) by the network's parameters of these standards (the throughput, the signal level) in different conditions. An experimental wireless network over 802.11ac standard was created and the authors simulated wireless network over 802.11n (5GHz) also in order to evaluate the benefits of IEEE 802.11ac and IEEE 802.11n (5GHz) wireless networks to the transmission of the telecommunication services. The investigation of Voice over Internet Protocol (VoIP) as a Real-time service, its quality parameters over wireless network was carried out. The simulation of VoIP service over 802.11n (5GHz) wireless network was made using Riverbed Modeler Academic Edition 17.5 software. The impact of the transmission of Non Real-time services (video streaming, FTP and HTTP) as an additional network traffic during the transmission of VoIP service was investigated also. The results of these investigations and the conclusions, based on the simulation and experimental investigations in the wireless networks over different 802.11ac and 802.11n (5GHz) standards, are presented in this paper.

GENERAL SPATIAL CORRELATION MODEL IN VON MISES ANGLE OF ARRIVAL DISTRIBUTION ENVIRONMENT

S. V. Savov and M. H. A. J. Herben **39**

Analytical expressions are derived for the envelope correlation of the signals measured with two closely spaced antennas in an urban multipath environment. The angles-of-arrival (AoA) of the multipath waves are assumed to be von Mises distributed. It are closed-form expressions and therefore easier to implement in for instance MIMO-capacity calculations than previously published formulas that include infinite summations. Moreover, the new expressions are not restricted to an array of isotropic radiators but also hold for an array of dipole antennas.

INFORMATION SYSTEM FOR MONITORING OF MAGNETIC INDUCTION IN MAGNETOTHERAPY

D. Dimitrov and V. Nikolov

The magneto-therapy is very often used actual method in medicine. It's important to be provided permanent monitoring of values of magnetic induction in every point around the human body and in the human body during the procedure of therapy. If one visualization of space distribution of values of magnetic induction in the patient's area would be available on line for the physician, he would be able to do optimization of process of therapy. One new system for magneto-therapy is "magnetic bed", which can provide therapy of every part of the human body separately. This system includes apparatus for magneto-therapy connected with many inductors around the human body. The system can provide "running" low frequency magnetic field using microprocessor unit in the apparatus for magneto-therapy. Special sensors situated in different points of the patient's area provided permanent information about the value of magnetic induction in these points. A microprocessor unit manages on line the process of measurement of magnetic induction in all points in patient's area and providing of computer image of space distribution of value of magnetic induction in the patient's area.

PLANE WAVE DIFFRACTION BY THE MULTILAYER STRUCTURE OF THE INFINITE 2D PERIODIC LATTICES

I. M. Petoev, V. A. Tabatadze, D. G. Kakulia, R. S. Zaridze

Tbilisi State University, Laboratory of Applied Electrodynamics,

3, Chavchavadze Ave. Tbilisi, Georgia

E-mail: ivanpetoev@gmail.com, E-mail: vasilitabatadze@gmail.com,

E-mail: dkakulia@gmail.com, E-mail: revaz.zaridze@lae.tsu.ge

Abstract

Plane electromagnetic wave diffraction problem on the multilayer structure of the infinite 2D periodic lattices is studied. The main goal of this investigation is to find the system parameters, for which it has the metamaterial properties - as the result of multiple resonances. The lattice element represents the conductor wire with small electric radius. There are considered the cases when this structure is embedded inside of the dielectric layer and also in the free space. For the first case the Method of Auxiliary Sources (MAS) is used. Interaction between several resonant layers amplifies metamaterial properties.

1. INTRODUCTION

Our investigations concern today's very topical problem - the metamaterials. In contrast to the standard dielectric materials, metamaterials at certain frequencies obtain interesting complex properties (chirality, negative refractive index and so on), so they are subject of practical interest. Generally, it is known that metamaterials could be obtained, if some periodic structure will be embedded in the conventional dielectric. Besides the many results, obtained in the world by other investigators, in the known to us literature, there is no any explanation of the mechanisms of these properties' appearance. Which phenomenon makes this consequence? Our investigation concerns to the determination of these kinds of mechanisms. It is well known that metamaterial properties appear only at some frequencies. According to our idea, it should be related to the multiple resonance

phenomena (when at the same frequency resonate the lattice elements and also the distance between these elements and the system in total are resonant).

Last years we had been working on the 3D finite size lattices, in order to confirm our idea [1]. Also we have considered just one infinite 2D periodic lattice in the free media and also inside of the dielectric layer [2, 3]. There were studied several cases, when the lattice element represents the conducting wire with small electrical radius and also the conducting plate [4]. Using the created computer program there was conducted numerical experiments and there was showed, that the appearance of the metamaterial's properties is really related to the multiple resonances phenomena. In particular, using computer simulation, by achieving the multiple resonances, there was obtained the chiral properties and negative refractive index, which are the properties of the complex materials. In this work there is studied several multilayer structures of the 2D infinite periodic lattices. By changing the distance between the layers, the resonant effects could be amplified. As a result of the computer simulation, there are found resonant parameters of the system, at which it has the negative refractive index. Changing any of the parameters of the system, the obtained property disappears, which highlights the validity of the multiple resonance idea.

2. THEORETICAL PART

2. 1. Problem statement.

At first let as consider the case, when the multilayer structure is located in a free space. This multilayer structure contains the finite amount of the infinite 2D lattices parallel to each other (figure 1). The lattice element represents the conducting wire with the small electrical radius. The lattices are shifted from each other with the same distances and this system is irradiated by the plane, harmonic in time electromagnetic wave. Our goal is to find the scattered field and investigate its properties.

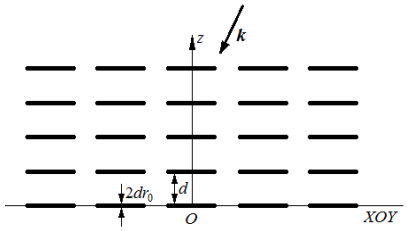

Figure 1. Multilayer structure's geometry

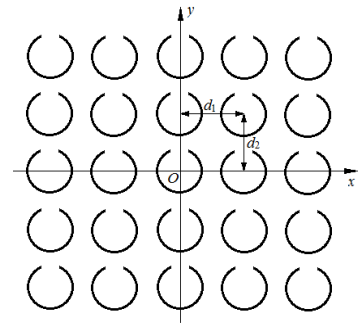

Figure 2. Zero layer

2. 2. Solution of the problem.

Let us choose the frame of reference so that the zero layer of the system is in $z=0$ plane (figure 2). For them in general we can write $z=z_\alpha=\alpha d$ where $\alpha=0,1,2,...,A$, d is the distance between two neighbor layers. d_1 and d_2 are the periods of these layers along the axis OX and OY. The plane wave falls from the $z>0$ semi-space and the direction of its propagation is determined by the wave vector $\vec{k}\left\{k_x,k_y,k_z\right\}$,

$$\vec{E}_{inc}\left(\vec{r}\right)=\vec{E}_0e^{i\vec{k}\vec{r}}\,,\vec{H}_{inc}\left(\vec{r}\right)=\vec{H}_0e^{i\vec{k}\vec{r}}\,,\ H_0=\sqrt{\varepsilon_0/\mu_0}E_0\,.$$

Here $\vec{r}\left\{x,y,z\right\}$ is the radius-vector of the observation point. The time dependence is $e^{-i\omega t}$. In order to solve this problem let us represent the unknown scattered field as:

$$\vec{E}\left(\vec{r}\right)=\sum_{\alpha=0}^{A}\vec{E}_\alpha\left(\vec{r}\right),\ \vec{H}\left(\vec{r}\right)=\sum_{\alpha=0}^{A}\vec{H}_\alpha\left(\vec{r}\right),$$

where $\vec{E}_\alpha\left(\vec{r}\right)$, $\vec{H}_\alpha\left(\vec{r}\right)$ represents the scattered field by the lattice which has the number α. In general the lattice element represents the continuously distributed elementary sources so we will have:

$$\vec{E}_\alpha\left(\vec{r}\right)=\int_{l_\alpha}I_\alpha\left(\vec{r}_\alpha\right)\vec{G}_E\left(\vec{r},\vec{r}_\alpha\right)dl_\alpha\,,\ \vec{H}_\alpha\left(\vec{r}\right)=\int_{l_\alpha}I_\alpha\left(\vec{r}_\alpha\right)\vec{G}_H\left(\vec{r},\vec{r}_\alpha\right)dl_\alpha\,,$$

where $I_\alpha\left(\vec{r}_\alpha\right)$- is the unknown function of the current distribution along the wire, excited in the element of interest. $\vec{G}_E\left(\vec{r},\vec{r}_\alpha\right)$ and $\vec{G}_H\left(\vec{r},\vec{r}_\alpha\right)$ are corresponding (periodical)

Green's functions, $\vec{r}_\alpha\{x_\alpha, y_\alpha, \alpha d\}$- is the variable radius-vector along this element. Therefore

$$\vec{E}(\vec{r}) = \sum_{\alpha=0}^{A} \int_{l_\alpha} I_\alpha(\vec{r}_\alpha) \vec{G}_E(\vec{r}, \vec{r}_\alpha) dl_\alpha, \ \vec{H}(\vec{r}) = \sum_{\alpha=0}^{A} \int_{l_\alpha} I_\alpha(\vec{r}_\alpha) \vec{G}_H(\vec{r}, \vec{r}_\alpha) dl_\alpha .$$

Green's function according to the [5] works should have the next form:

$$\vec{G}_E(\vec{r}, \vec{r}_\alpha) = (1/2\omega\varepsilon_0\varepsilon d_1 d_2) \sum_{m=-\infty}^{+\infty} \sum_{n=-\infty}^{+\infty} e^{i\vec{k}_{\alpha,mn}(\vec{r}-\vec{r}_\alpha)} \left(\mu\varepsilon k^2 - k_{n,x}^2 - k_{m,y}^2\right)^{-1/2} \left(\vec{k}_{\alpha,mn} \times \left(\vec{k}_{\alpha,mn} \times d\vec{l}_\alpha\right)\right),$$

$$\vec{G}_H(\vec{r}, \vec{r}_\alpha) = (1/2 d_1 d_2) \sum_{m=-\infty}^{+\infty} \sum_{n=-\infty}^{+\infty} e^{i\vec{k}_{\alpha,mn}(\vec{r}-\vec{r}_\alpha)} \left(\mu\varepsilon k^2 - k_{n,x}^2 - k_{m,y}^2\right)^{-1/2} \left(d\vec{l}_\alpha \times \vec{k}_{\alpha,mn}\right),$$

$$\vec{k}_{\alpha,mn} = k_{n,x}\vec{x} + k_{m,y}\vec{y} + \operatorname{sgn}(z - \alpha d)\sqrt{\mu\varepsilon k^2 - k_{n,x}^2 - k_{m,y}^2}\,\vec{z},$$

$$k_{n,x} = k_x + 2\pi n/d_1, \ k_{m,y} = k_y + 2\pi m/d_2 .$$

In these expressions ε, μ - are the permittivity and permeability of the media (as the multilayer structure in the first case is in the vacuum so $\varepsilon = \mu = 1$). For the unknown current distribution $I_\alpha(\vec{r}_\alpha)$ we satisfy the boundary condition and get the equation:

$$d\vec{l}_\beta \cdot \sum_{\alpha=0}^{A} \int_{l_\alpha} I_\alpha(\vec{r}_\alpha) \vec{G}_E(\vec{r}_\beta + d\vec{r}_0, \vec{r}_\alpha) dl_\alpha = -d\vec{l}_\beta \cdot \vec{E}_0 e^{i\vec{k}(\vec{r}_\beta + d\vec{r}_0)} .$$

During the numerical calculations the integral should be replaced by the finite sum:

$$\vec{E}(\vec{r}) = \sum_{\alpha=0}^{A} \sum_{j=1}^{N} I_{\alpha j} \vec{G}_E(\vec{r}, \vec{r}_{\alpha j}), \qquad \vec{H}(\vec{r}) = \sum_{\alpha=0}^{A} \sum_{j=1}^{N} I_{\alpha j} \vec{G}_H(\vec{r}, \vec{r}_{\alpha j}) \tag{1}$$

here $I_{\alpha j} = I_\alpha(\vec{r}_\alpha) dl_{\alpha j}$ - is unknown current amplitude, which is considered as constant along small $dl_{\alpha j}$ segment. First α index indicates the number of the lattice, and the second j index - the segment number in the element. From the boundary condition we get linear algebraic equation system with respect to the unknown coefficients $I_{\alpha j}$:

$$d\vec{l}_{\beta p} \cdot \sum_{\alpha=0}^{A} \sum_{j=1}^{N} I_{\alpha j} \vec{G}_E(\vec{r}_{\beta p} + d\vec{r}_0, \vec{r}_{\alpha j}) = -d\vec{l}_{\beta p} \cdot \vec{E}_0 e^{i\vec{k}(\vec{r}_{\beta p} + d\vec{r}_0)},$$

where $\beta = 0, 1, 2, ..., A$, $p = 1, 2, ..., N$.

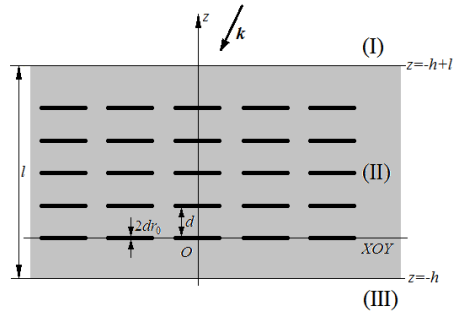

Figure 3. Multilayer structure in dielectric

Now let us consider the case, when the above mentioned multilayer structure is located in the dielectric layer, infinite along the OX and OY axes, with the l width along the OZ axis. This layer is bounded with the surfaces $z=-h$, $z=-h+l$ and has ε permittivity and μ permeability. l width must be bigger than Ad. Our goal is to study the scattered field dependence on the resonant parameters of the system in the (I) - (III) areas (figure 3).

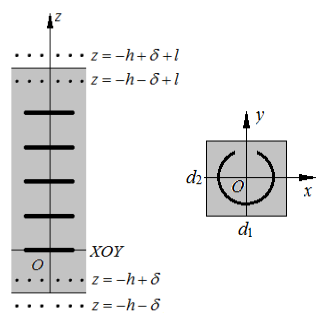

Figure 4. The geometry of structure within one period

In order to find the scattered field, in this case we have to use the Method of Auxiliary Sources (MAS) [1]. In order to determine the scattered field in each areas of the interest, we consider 4 auxiliary surfaces: $z=-h-\delta$, $z=-h+\delta$, $z=-h-\delta+l$, $z=-h+\delta+l$, where δ represents the distance between the auxiliary surface and the dielectric surface. Because of the periodicity of the field we investigate it only in the points where $(x,y)\in(d_1\times d_2)$ (figure 4). The second and the third auxiliary surfaces are inside of the layer and describe the field outside. Other two surfaces are outside of the layer and they describe the field inside of the layer. The auxiliary sources are two mutual perpendicular dipoles, the polarization of which coincides to the $\vec{x}$ and $\vec{y}$ basis vectors.

The field of such dipole in general is described by the periodical Green function. The field of the auxiliary source in general has to be written as: $a_\nu \vec{G}_E^x(\vec{r},\vec{r}_\nu)+b_\nu \vec{G}_E^y(\vec{r},\vec{r}_\nu)$, where upper x and y indices determine the dipole polarizations, and a_ν and b_ν represent their unknown amplitudes. This expression can be written compactly as:

$$a_\nu \vec{G}_E^x(\vec{r},\vec{r}_\nu)+b_\nu \vec{G}_E^y(\vec{r},\vec{r}_\nu)=A_\nu \vec{G}_E^{x,y}(\vec{r},\vec{r}_\nu).$$

In the area (I) (figure 3) the total field represents the sum of the incident field and the field represented by the $z=-h-\delta+l$ auxiliary surface:

$$\vec{E}_{(I)}(\vec{r})=\vec{E}_0 e^{i\vec{k}\cdot\vec{r}}+\sum_\nu A_\nu \vec{G}_E^{x,y}(\vec{r},\vec{r}_\nu),\ \vec{H}_{(I)}(\vec{r})=\vec{H}_0 e^{i\vec{k}\cdot\vec{r}}+\sum_\nu A_\nu \vec{G}_H^{x,y}(\vec{r},\vec{r}_\nu) \tag{2}$$

where $(\vec{r}_\nu)_z=-h-\delta+l$, $\mu=\varepsilon=1$.

In the area (II) the total field is described by the field scattered by the layers and also by the fields represented with the $z=-h-\delta$, $z=-h+\delta+l$ auxiliary surfaces:

$$\begin{aligned}\vec{E}_{(II)}(\vec{r})&=\sum_{\alpha=0}^{A}\sum_{j=1}^{N} I_{\alpha j}\vec{G}_E(\vec{r},\vec{r}_{\alpha j})+\sum_\nu B_\nu \vec{G}_E^{x,y}(\vec{r},\vec{r}_\nu)+\sum_\sigma C_\sigma \vec{G}_E^{x,y}(\vec{r},\vec{r}_\sigma),\\ \vec{H}_{(II)}(\vec{r})&=\sum_{\alpha=0}^{A}\sum_{j=1}^{N} I_{\alpha j}\vec{G}_H(\vec{r},\vec{r}_{\alpha j})+\sum_\nu B_\nu \vec{G}_H^{x,y}(\vec{r},\vec{r}_\nu)+\sum_\sigma C_\sigma \vec{G}_H^{x,y}(\vec{r},\vec{r}_\sigma),\end{aligned} \tag{3}$$

where: $(\vec{r}_\nu)_z=-h-\delta$, $(\vec{r}_\sigma)_z=-h+\delta+l$.

In the area (III) we have only transmitted field, which is described by the $z=-h+\delta$ auxiliary surface:

$$\vec{E}_{(III)}(\vec{r})=\sum_\nu D_\nu \vec{G}_E^{x,y}(\vec{r},\vec{r}_\nu),\ \vec{H}_{(III)}(\vec{r})=\sum_\nu D_\nu \vec{G}_H^{x,y}(\vec{r},\vec{r}_\nu), \tag{4}$$

where: $(\vec{r}_\nu)_z=-h+\delta$, $\mu=\varepsilon=1$.

Determination of the unknown amplitudes is possible by the satisfaction of the boundary conditions as on the dielectric surfaces also along the layer elements:

$$\begin{cases}\vec{E}_{(I)}(\vec{r})\big|_{z=-h+l}\vec{\tau}=\vec{E}_{(II)}(\vec{r})\big|_{z=-h+l}\vec{\tau},\ \vec{H}_{(I)}(\vec{r})\big|_{z=-h+l}\vec{\tau}=\vec{H}_{(II)}(\vec{r})\big|_{z=-h+l}\vec{\tau},\\ \vec{E}_{(II)}(\vec{r})\big|_{z=-h}\vec{\tau}=\vec{E}_{(III)}(\vec{r})\big|_{z=-h}\vec{\tau},\ \vec{H}_{(II)}(\vec{r})\big|_{z=-h}\vec{\tau}=\vec{H}_{(III)}(\vec{r})\big|_{z=-h}\vec{\tau},\ \vec{E}_{(II)}(\vec{r})d\vec{l}=0.\end{cases}$$

Here $\vec{\tau}$ and $d\vec{l}$ are the tangential vectors on the dielectric surface and on the lattice element. After the solution of this system we find the unknown (1) – (4) scattered field.

3. RESULTS OF THE NUMERICAL EXPERIMENTS

3. 1. Evaluation of the solution accuracy.

For validation of the proposed algorithm, there was considered the simple problem of the plane wave incidence on the planar surface of the vacuum-glass, with the refractive index n_2=1.52, (figure 5). Obtained dependence of the reflection coefficients on the incidence angle for two cases of incident wave polarization are in good coincidence with the same result obtained by Fresnel's formulas.

During computer simulation, at first, we have checked the exactness of the proposed algorithm in order to find optimal values of the auxiliary parameters in the units of the incident wave length: dr_0/λ - the radius of the lattice elements' cross-section; N/λ and N/λ^2 - the number of the collocation points along the element and on the layer surface; δ/λ - the distance between the real and auxiliary surfaces.

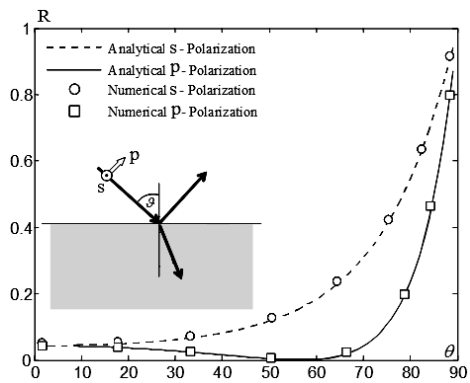

Figure 5. Dependence of reflection on incidence angle

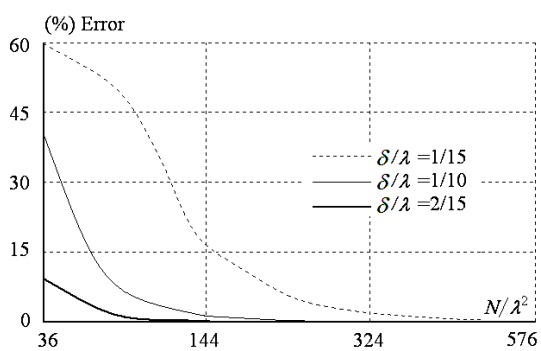

Figure 6. Deviation from the boundary condition satisfaction on the layer surface depended on the collocation points number

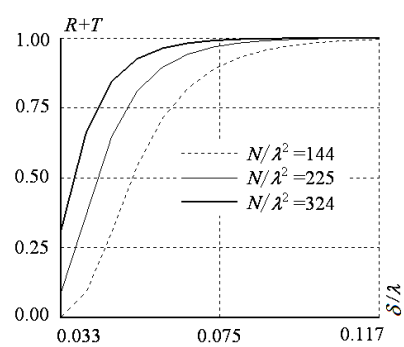

Figure 7. Dependence of the balance exactness $R+T$=1 on the shift δ/λ

Figure 6 shows the errors of the boundary conditions satisfaction on the dielectric surface, depended on the collocation point number, for different distances of the auxiliary surfaces. As we see 36 points on the wave length squared gives the error smaller than 10% for the auxiliary distance $\delta/\lambda = 2/15$, in case of the $\delta/\lambda = 1/10$, 144 points (12 points on the wave number) gives the error 2%. In the given case perpendicularly oriented incident plane wave is polarized along the axis OX. The algorithm is checked also by the balance estimation of the reflection and transmission coefficients: $R+T=1$, which comes from the energy conservation law. On the figure 7 there is presented the energy balance dependence on the δ/λ auxiliary parameter, for three different values of the number N/λ^2. As we see, the energy balance is well satisfied for 144 points (12 points per λ), if $\delta/\lambda > 0.075$.

3. 2. Numerical results.

Before this investigation, we have studied the resonant properties of the 3D finite size lattices [1]. There was considered the case, when the lattice element represents two open conductor rings with radiuses R and $r = 0.5R$ as it is shown on figure 8, 9.

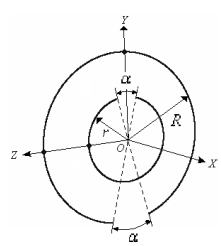

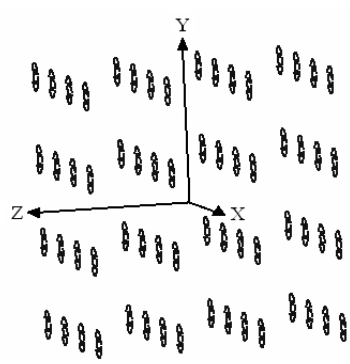

Figure 8. The lattice element Figure 9. The periodic structure

Solving the diffraction problem on this structure, there were found the resonant parameters of the system, when it has the metamaterial properties with negative refraction index. these parameters are: $R = 0.14\lambda$, $r = 0.07\lambda$ and the lattice periods $d_1 = d_2 = d_3 = 0.86\lambda$, where λ - represents the incident wave length.

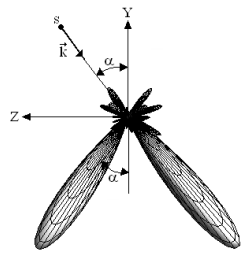

Figure 10. The far field pattern

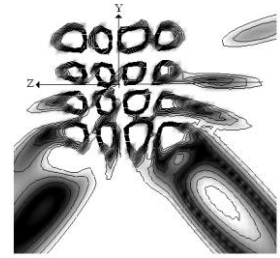

Figure 11. The near field distribution

On the figure 10 there is presented the far field pattern. The main lobe has the direction of the incident field. The second lobe represents the negative refraction. On the figure 11 is presented the corresponding near field distribution. Here we can see that the second lobe, as well as the main lobe is formed inside of the structure. If we change the incident frequency, or some structure parameter, the second lobe disappears, which also highlights the resonant character of this phenomenon. In order to amplify this negative refraction effect, the number of lattice elements should be increased. Therefore is interesting to consider the infinite multilayer structures.

Next there are presented the results of investigations for infinite multilayer structure. The number of layers is 5. Each layer is parallel to the *XOY* plane. Lattice element also represents two open conductor rings (figure 8). The numerical experiments show that in order to get negative refraction effect, the structure parameters should have the values $d_1 = d_2 = 0.86\lambda$, $d = 0.86\lambda$, $R = 0.14\lambda$, $r = 0.07\lambda$ (figure 3), which coincide with the corresponding parameters for the finite lattice. It must be mentioned that we didn't get the negative refraction in case of less layers number. The incident planar wave propagates along $\vec{k}$ vector and falls with the angle 45^0.

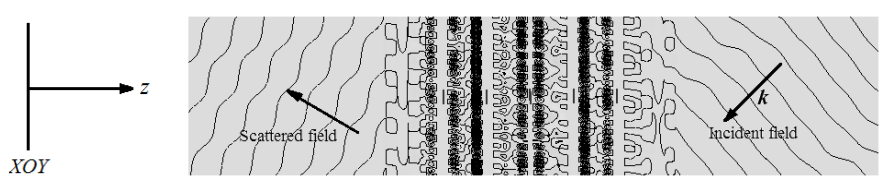

Figure 12. The near field in resonant case

On figure 12 there is presented the near field distribution in *XOZ* section. As we can see, the near field between the layers is resonant and as a result, scattered field in transmitted area has negative refraction direction. The figure 13 represents the near field

distribution when the distant between the layers doesn't have the resonant value: $d = 0.56\lambda$. In this case the negative refraction disappears. Finally, in case of one layer we also can't get the negative refraction (figure 14).

Figure 13. The near field in non resonant case

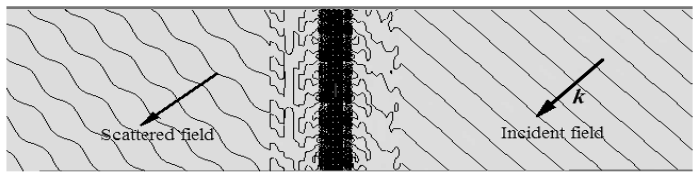

Figure 14. The near field in case of one layer

The numerical experiments show that the negative refraction property is observed for the distance values d, which belongs to the interval $0.670\lambda < d < 1.018\lambda$. On the figures 15 and 16 are presented the near field distributions when $d = 0.670\lambda$ and $d = 1.018\lambda$.

Figure 15. The near field distribution. d=0.670λ

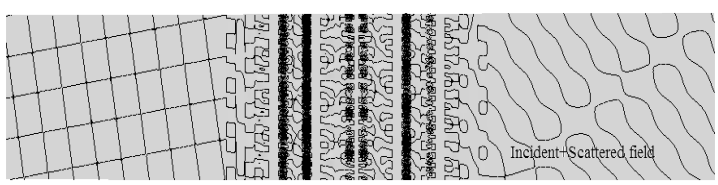

Figure 16. The near field distribution. d=1.018λ

In the transmitted area we can see the rectangular contour lines which in reality represent the superposition of two wave fronts, with the negative and positive refraction directions. According to the numerical experiments, where the distance between the layers changes in the range $0.670\lambda < d < 1.018\lambda$, we have only negative refraction.

4. CONCLUSION

The plane electromagnetic wave diffraction problem on the multilayer structure, which consists of the 2D periodical infinite equidistant lattices was considered in order to obtain the metamaterial's properties at some resonant frequencies. Using the computer simulation of the stated problem and realization of the numerical calculations, there are found resonant parameters of the system, at which it has the negative refractive index, which corresponds to the certain kind of metamaterial. Changing any of the parameters of the system, the obtained property disappears, which highlights the validity of the multiple resonance's idea - as the main mechanism for metamaterial property's appearance.

ACKOWLEDGMENT

The work is done with the financial support of the Shota Rustaveli National Science Foundation in the Scope of the grant 52/15.

REFERENCES

[1] I. M. Petoev, V. A. Tabatadze, R. S. Zaridze, "The Method of Auxiliary Sources Applied to Problems of Electromagnetic Wave Diffraction by Certain Metal–Dielectric Structures". Journal of Communications Technology and Electronics, Vol. 58, No. 5, 2013, pp. 404-416.

[2] I. M. Petoev, V. A. Tabatadze, D. G. Kakulia, R. S. Zaridze, "Application of the Method of Auxiliary Sources on the 2-D Periodic Lattice". Journal of Applied Electromagnetism (JAE), Vol. 14, No.2, 2012, pp. 39-55.

[3] I. Petoev, V. Tabatadze, R. Zaridze. "The Electromagnetic Properties of the Infinite Periodic Lattice Embedded in the Dielectric Layer. Localization of the Inhomogeneity in two-way Line". Proceedings of XVI-th International Seminar/Workshop on Direct and Inverse Problems of Electromagnetic and Acoustic Wave Theory (DIPED-2011), September 26-29, 2011, Lviv, Ukraine. pp. 39-45.

[4] I.M. Petoev, V.A. Tabatadze, D.G. Kakulia, R. S. Zaridz, "Application of the Method of Auxiliary Sources for the Thin Plates and Open Surfaces". Journal of Communications Technology and Electronics, 2013. Accepted for publication.

[5] G. Kevanishvili, D. Bakradze, K. Kotetishvili, "Summation of the Double Row in the Theory of Wave Diffraction by the 2D Periodic Planar Lattices", Georgian Engineering News, September 1997, pp. 3-9.

[6] I. M. Petoev, V. A. Tabatadze, R. S. Zaridze, "The Double and Triple Resonances Investigation for the "Cassini" Lattice Into the Dielectric". Journal of Applied Electromagnetism (JAE), Vol.15, No.2, 2013, pp. 8-27.

HOMOMORPHIC FILTERING APPROACH FOR NARROW BAND IMAGES ENHANCEMENT

V. M. Georgieva

Faculty of Telecommunications, Technical University of Sofia, Bulgaria

1000 Sofia, "Kl. Ohridsky" str.8

E-mail: vesg@tu-sofia.bg

Abstract

The application of narrow band imaging (NBI) in endoscopy improves the accuracy in diagnosis, including reduction in cost and time. It allows better definition between the epithelial surface and the adjacent vascular net via the application of narrow-bandwidth filters to standard white-light endoscopy. The fact, that only selected bandwidths are emitted results in a lower brightness, which requires special high –sensitive dual mode CCDs.

In the paper is presented an approach for NB images enhancement using improved homomorphic filtering. Traditional homomorphic filtering is based on Fourier transform, which has higher resolution in frequency domain and lower resolution in spatial domain. The proposed algorithm includes homomorphic filtering based on wavelet packet transform as first step of improving, and contrast limited adaptive histogram equalization (CLAHE) as the second improving step to adjust its whole luminousness. An adaptive threshold estimation method for image denoising in the wavelet domain is used, for modeling of detail sub-band coefficients. An effective algorithm was treatment by optimization of some parameters of the CLAHE and wavelet transformation on the base of objective quantitative estimation parameters. The main goal is noise reduction and improving the quality of the diagnostic images.

Some results of the experiments with colonoscopy images are presented, which were made by computer simulation in MATLAB environment.

1. INTRODUCTION

Narrow Band Imaging (NBI) uses scattering and absorption properties of human tissue. The penetration depth before being scattered (partly absorbed) depends on the wavelength (colour) of the light. The shorter the wavelength (e.g. blue 415 nm), the earlier it is reflected. Longer wavelengths (e.g. green 540 nm) penetrate deeper. In other words, the image obtained through white light is a composition of slightly different tissue layers. A bright but partially blurred image is the result. Narrow band imaging (NBI) enhances the visualisation of the capillary network and mucosal morphology during endoscopic observation of the gastrointestinal tract. The result is

an image with focus on super ficial mucous layers (blue) and the capillary network of the deeper submucosal layer (green). This provides improved visual contrast of the surface structure and fine capillary patterns of the mucous membranes [1] .

The fact that only selected bandwidths are emitted results in a lower brightness which requires special high-sensitive dual mode CCDs. The principle of narrow band imaging technology is presented in Figure 1.

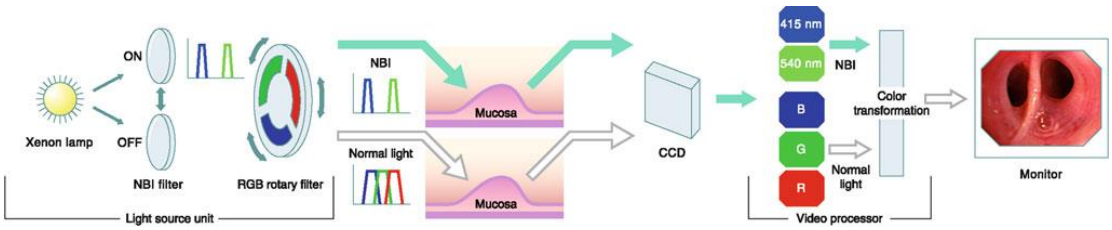

Figure 1. Principle of narrow band imaging technology

Homomorphic filtering can eliminate the nonuniformity luminance distribution of image, and keep its original state. But the property of local spatial domain has not been considered. As a result, enhancement in local contrast is poor. Moreover, the operational speed with the method of homomorphic filtering based on Fourier transform is slower relatively, and it takes up more operational time and space [2].

Wavelet transform has been used in digital image processing widely because of its individual characters, such as multiscale, spatial localization and frequency localization. By this way, both low frequency smooth sub-image and high frequency detailed sub-image with different scale could be obtained [3]. And according to different characters of original image, different coefficient will be used to enhance it [4]. Because of these weakness of traditional homomorphic filtering above, wavelet transform was used instead of Fourier transform to improve operational efficiency. And histogram equalization could be done on image to increase its local contrast [5].

In the paper is presented another approach, homomorphic filtration and noise reduction on the base of wavelet packet transformation (WPT) and contrast limited adaptive histogram equalization (CLAHE). Some quantitative estimation parameters: Noise reduction ratio (NRR), Signal to noise ratio in the noised image (SNR_Y), Signal to noise ratio in the filtered image (SNR_F), Effectiveness of filtration (E_{FF}), Peak signal to noise ratio (PSNR) have been analyzed in the paper.

2. BASIC STAGES OF THE ALGORITHM

2.1. Homomorphic Filtering based on WPT

The standard homomorphic filtering uses illumination-reflectance model in its operation. This model consider the image is been characterized by two primary components. The first component is the amount of source illumination incident on the scene being viewed $i(x,y)$. The second component is the reflectance component of the objects on the scene $r(x,y)$. The image $f(x,y)$ is then defined as [6-8]:

$$f(x, y) = i(x, y)r(x, y) \tag{1}$$

In this model, the intensity of $i(x,y)$ changes slower than $r(x,y)$. Therefore, $i(x,y)$ is considered to have more low frequency components than $r(x,y)$. Using this fact, homomorphic filtering technique aims to reduce the significance of $i(x,y)$ by reducing the low frequency components of the image. This can be achieved by executing the filtering process in frequency domain. However, before the transformation is taking place, logarithm function has been used to change the multiplication operation of $r(x,y)$ with $i(x,y)$ in Eq.(1) into addition operation.

$$z(x, y) = \ln f(x, y) = \ln i(x, y) + \ln r(x, y) \tag{2}$$

In the Fourier transform of traditional homomorphic filtering, spatial resolution is lower, and local contrast of image is not increased obviously. Lowpass filtering could reduce noise by smoothing, but the border of image will become to more indistinct. Highpass filtering could enhance the edge of image, but the noise of background will be increased.

Using Fourier transform, the standard homomorphic filtering schema can be presented in Figure 2, where DFT is 2D Discrete Fourier Transform, H(u,v) is a filter function, $(DFT)^{-1}$ is 2D Inverse Discrete Fourier Transform and $g(x,y)$ is the output image. Using Wavelet packet transform, block DFT will be changed with WPT and block $(DFT)^{-1}$ with IWPT.

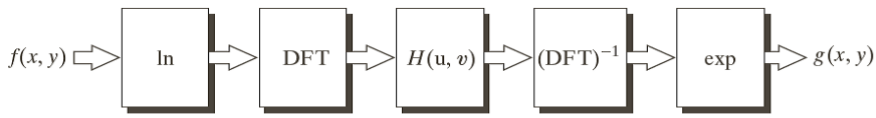

Figure 2. The flowchart of homomorphic filtering

The method can propose more complete analysis and provides increased flexibility according to DWT. It has the following important properties:

- A richer presentation of the image, basic on functions with wavelet forms, which consist of 3 parameters: position, scale and frequency of the fluctuations around a given position;
- Numerous decompositions of the image, that allows estimate the noise reduction of different levels of its decomposition;
- Adaptive noise reduction on each level of the decomposition by choice of best tree decomposition and optimal thresholds parameters.

Because the noise of wavelet transform usually concentrate on the state of high resolution, the method is useful to eliminate the noise.

2.2. Noise reduction on the base of 2D wavelet packet transformation

The wavelet packet analysis is a generalization of wavelet decomposition that offers a richer image analysis. Based on the organization of the wavelet packet library, it can be determinate the decomposition issued from a given orthogonal wavelets. As this number can be very large, it is interesting to find an optimal decomposition with respect to a conventional criterion. The classical entropy-based criterion by Shannon is a common concept. [9].

Looking for best shrinkage decomposition to noise reduction, two important conditions must be realized together [10]. The conditions are following:

$$E_K(S) = \min, \quad for\, K = 1,2,3...n \quad , \tag{3}$$

where E_K is the entropy in the level K for the best tree decomposition of image S

$$s_{ij} \geq T \, , \tag{4}$$

where s_{ij} are the wavelet coefficients of S in an orthonormal basis, T is the threshold of the coefficients.

By determination of the global threshold it is used the strategy of Birge-Massart [11].

This strategy is flexibility. It used spatial adapted threshold that allows to determinate the threshold in three directions: horizontal, vertical and diagonally. In

addition the threshold can be hard or soft. It is proposed to use in addition the Normal Shrink method to calculate the threshold value (T_N) only for the detail sub-bands in the best shrinkage decomposition. This threshold can be adaptive and calculated to different sub-band characteristics [12]:

$$T_N = \frac{\beta\sigma^2}{\sigma_Y} \ , \tag{5}$$

where the scale parameter β is computed once for each scale using the following equation:

$$\beta = \sqrt{\log\left(\frac{L_M}{J}\right)} , \tag{6}$$

where L_M is the length of the sub-band at M^{th} scale, J is number of decompositions, σ_Y is the standard deviation of the sub-band under consideration computed by using the standard MATLAB command.

2.3. Contrast limited adaptive histogram equalization (CLAHE)

Contrast limited adaptive histogram is a technique utilized for improving the local contrast of images. It is a generalization of ordinary histogram equalization and adaptive histogram equalization. CLAHE does not operate on the whole image works like ordinary Histogram Equalization (HE), but it works on small areas in images, named tiles. Each tile's contrast is enhanced, so that the histogram of the output area roughly matches the histogram determined by the 'Distribution' parameter. The adjacent tiles are then combined using bilinear interpolation to eliminate artificially induced boundaries. The algorithm CLAHE limits the slope associated with the gray level assignment scheme to prevent saturation. This process is accomplished by allowing only a maximum number of pixels in each of the bins associated with the local histograms. After “clipping” the histogram, the clipped pixels are equally redistributed over the whole histogram to keep the total histogram count identical. The procedure of CLAHE is applied to Y component of the selected image that is processing in YUV system as more effectiveness.

3. EXPERIMENTAL RESULTS

The formulated stages of processing are presented by computer simulation in MATLAB, version 8.1 environment with using the IMAGE PROCESSING and WAVELET TOOLBOXES. In analysis are used 20 NB images with size 768x576 from colonoscopy. The original images have been done in jpeg file format. By post processing they are converted in YUV system and bmp format.

The obtained average results from the simulation are presented in Table 1.

Table 1. Simulation results of different methods for pre-processing of NB images

Basic stages of processing	PSNR **[dB]**	SNR_Y **[dB]**	SNR_F **[dB]**	E_{FF} **[dB]**
Homom. filtering based on WPT	32.7106	18.9512	20.8413	1.8901
CLAHE	33.1274	-	-	-

The obtained results from the simulation show that the homomorphic filtering on the base of wavelet packet transformation by using of adaptive threshold estimation method is an effective approach. The values of PSNR and Effectiveness of filtration (E_{FF}) are significant and the value of NRR is about 0.3, and shows that the noise is about three times reduced. The variances of the estimations parameters are about ±0.01 by the particular images and depend on quality of the different image.

On Figure 3 is presented the original NB image. In Figure 4 and Figure 5 are shown the filtered image and the image after contrast enhancement respectively. The calculated histograms of the original and processed image are presented in Figure 6.

The obtained results can be compared with other methods such as standard homomorphic filtering and homomorphic filtering on the base on and 2D discrete wavelet transformation (DWT). The obtained average results from the simulation of are presented in Table 2.

Table 2. Simulation results of different methods for homomorphic filtering of NB image

Method of pre-processing	**PSNR [dB]**	**NRR**	SNR_Y **[dB]**	SNR_F **[dB]**	E_{FF} **[dB]**
Standard HF	29.4573	0.6598	18.9512	19.5183	0.8671
HF on the base of DWT	30.9819	0.5094	18.9512	20.1222	1.1710
HF on the base of DWPT	32.7106	0.3341	18.9512	20.8413	1.8901

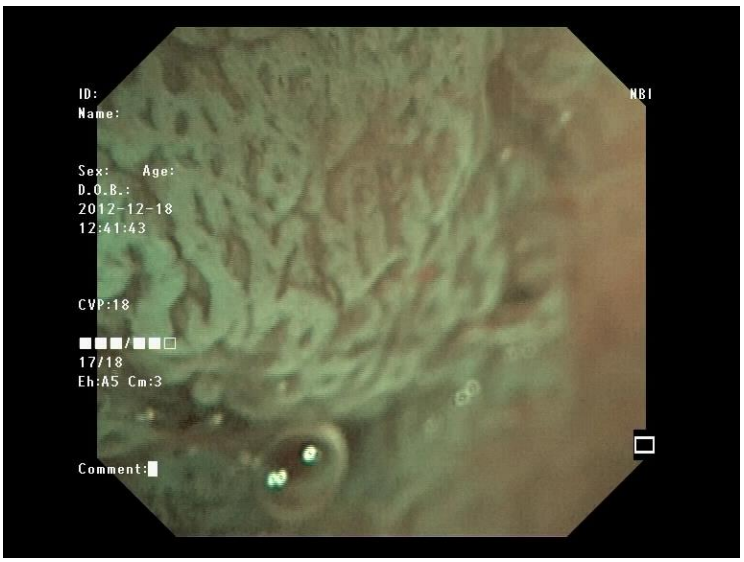

Figure 3. The original colonoscopy image

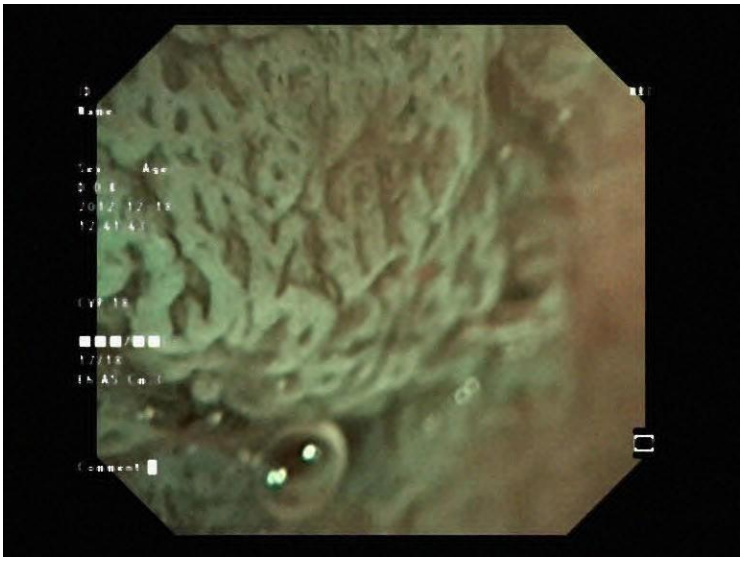

Figure 4. The image after homomorphic filtering on the base on DWPT

Figure 5. The image after CLAHE

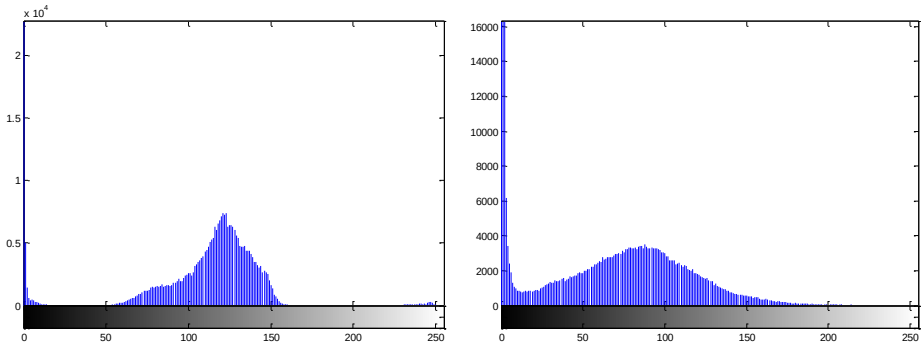

a) b)

Figure 6. Histograms of Y component of NB images: a) original; b) processed

The graphical presentations of the obtained results for PSNR and E_{FF} are given on Figure 7.

Figure 7. Diagrams of E_{FF} and PSNR

The obtained simulation results show that the proposed method is more effectiveness. The value of NRR is about 0.3 and shows that the noise is three times

reduced. The value of NRR by second method, based on DWT is about 0.5 and shows that the noise is two times reduced. The values of PSNR and Effectiveness of filtration (E_{FF}) for the proposed method are more sufficient. The experimental results showed enhancement of the image and increasing of image information in consequence of brightness level restoration.

5. CONCLUSION

In the paper is proposed a new and effective approach for NB image enhancement, based on improvement of homomorphic filtering. The complex processing has an effect of brightness and contrast enhancement, noise reduction on the base of WPT, that results in clear vision of the mucosa in colonoscopy images. An adaptive threshold estimation method for noise reduction in the wavelet domain is used, based on combination of threshold strategy of Birge-Massart and Normal Shrink method for modeling of detail sub-band coefficients. The implemented investigation and obtained results by using real NB images attempt to make diagnostic more obvious. The proposed technique can be helpful for detection and classification of superficial neoplastic lesions.

REFERENCES

[1] Harald W. Dremel ”General Principles of Endoscopic Imaging”, Principles and Practice of Interventional Pulmonology, Springer Science+Business Media New York, pp. 15- 25, 2013

[2] Wen Sha, You Zhi-sheng, “A performance optimized algorithm of spatial domain homomorphic filtering,” Application Research of Computers, Vol.173, pp. 62-65, 2000.

[3] Zong x, Laine AF, and Geiser EA, “Speckle reduction and contrast enhancement of echocardiograms via multiscale nonlinear processing,” IEEE Transactions on Medical Imaging,Vol.174, pp. 532-540, 1998.

[4] Zhang C, Wang X, Wang J, et al, “Contrast enhancement for image based on discrete stationary wavelet transform,” International Society for Optical Engineering, US, pp. 01-08, 2005.

[5] Wenli Liu, Peng He, Hui Li, Hongbo YuH.,” Improvement on the Algorithm of Homomorphic Filtering”, Advances in Biomedical Engineering, Vol.11, pp.120- 124, 2012

[6] C.-N. Fan and F.-Y. Zhang, "Homomorphic filtering based illumination normalization method for face recognition," Pattern Recognition Letters, vol. 32, pp. 1468-1479, 2011.

[7] A. Holger G, "Butterworth equations for homomorphic filtering of images," Computers in Biology and Medicine, vol. 28, pp. 169-181, 1998.

[8] K. Delac, et al., "Sub-image homomorphic filtering technique for improving facial identification under difficult illumination conditions," Proc. 13th International Conference on Systems, Signals and Image Processing, pp. 95-98, 2006,

[9] R.Coifmann, M.Wickerhauser, “Entropy based Algorithms for best basis selection”, IEEE Transaction on information theory, Vol.38, pp.713-718, 1992.

[10] V.Georgieva, R.Kountchev, “An influence of the wavelet packet decomposition on noise reduction in ultrasound images”, Proceedings of International Scientific Conference on Information, Communication and Energy Systems and Technology, pp.185-188, Sofia, Bulgaria, 2006.

[11] MATLAB, User’s Guide, www.mathwork.com

[12] L. Kaur, S., Gupta, R. Chauhan, “Image denoising using wavelet thresholding”, Journal of Medical Engineering Technology, Vol.29, pp.208-214, 2006

IEEE 802.11AC STANDARD IMPACT ON TRANSMISSION OF VOIP SERVICE
(the experimental look towards the growth of users' mobility)

(Paper selected from CEMA'14 Conference)

A. Matusevičius, T. Adomkus, L. Narbutaite, R. Bruzgiene

Department of Telecommunications,
Faculty of Electrical and Electronics engineering,
Kaunas University of Technology,
Studentų str. 50-452, Kaunas, LT- 51368, Lithuania
E-mail: tomas.adomkus@ktu.lt

Abstract

In our days practically all users want to have a connection to a wireless network not only at home, but in any place at any time. So, the users want that their network devices as much as possible be mobile and at the same time ensure high Quality of Services (QoS). Local wireless networks (WiFi) are good choice for the users' mobility, however it have a number of disadvantages, as the limited network's bandwidth and the pollution of the radio ether. That is the reason for 5 GHz frequency use as it is clearer comparing with 2.4 GHz frequency range. More flexible and more adaptable wireless networks, based on a 5 GHz frequency range are IEEE802.11n (5GHz) and IEEE 802.11ac. The wireless networks over 5 GHz frequency range are more advanced due to the more clear radio ether and improved network's bandwidth. According to this, the authors compared 802.11ac with 802.11n (5GHz) by the network's parameters of these standards (the throughput, the signal level) in different conditions. An experimental wireless network over 802.11ac standard was created and the authors simulated wireless network over 802.11n (5GHz) also in order to evaluate the benefits of IEEE 802.11ac and IEEE 802.11n (5GHz) wireless networks to the transmission of the telecommunication services. The investigation of Voice over Internet Protocol (VoIP) as a Real-time service, its quality parameters over wireless network was carried out. The simulation of VoIP service over 802.11n (5GHz) wireless network was made using Riverbed Modeler Academic Edition 17.5 software. The impact of the transmission of Non Real-time services (video streaming, FTP and HTTP) as an additional network traffic during the transmission of VoIP service was investigated also. The results of these investigations and the conclusions, based on the simulation and experimental investigations in the wireless networks over different 802.11ac and 802.11n (5GHz) standards, are presented in this paper.

1. INTRODUCTION

Currently, the real-time services and the wireless networks (Wi-Fi) are very popular and widely used [1, 2]. However, these real-time services have very strict requirements for their quality characteristics [3]. The latter are directly dependent on the channel bandwidth. This problem was solved with the new next generation 802.11ac standard [4-6]. IEEE 802.11ac wireless standard is able to provide a theoretical data rate of 3.5 Gbps with the channel width of 160 MHz for 4 streams at 256-QAM modulation. This is indeed an impressive speed compared to the 802.11n standard, which is currently widely in use now [7]. IEEE 802.11n standard provides a maximum theoretical data rate of 1.3 Gbps.

In order to compare the 802.11n and 802.11ac wireless standards in theoretical and practical view, the simulation and experiments of it throughput, the signal strength are presented in this paper. Then, to make sure that the 802.11ac standard is able to transmit multiple streams of a real-time service, the authors carried out the experiments, which investigate the quality of VoIP service, continuously increasing the number of active TCP sessions in the network. The results of these investigations and the conclusions are presented in this paper.

2. COMPARATIVE ANALYSIS OF SIMULATED PARAMETERS OVER IEEE 802.11N AND 802.11AC WIRELESS NETWORKS

In order to evaluate the possibility of the user as a mobile user of a wireless network, it is necessary to compare two different IEEE 802.11n and 802.11ac standards in accordance to their signal coverage and throughput. The authors used *Ekahau Site Survey* software tool for the simulation of throughput and received signal strength in the wireless networks based on 802.11n and 802.11ac standards. The selected access point (AP) is working on 802.11n and 802.11ac standards in 5GHz frequency band. The simulation was done in LOS (Line of Sight) and NLOS (Non-Line of Sight) conditions of the wireless networks. It has been used the wall of a 20 cm thick in NLOS conditions. The comparison of the throughput by using the different wireless standard is presented in Figures 1 and 2.

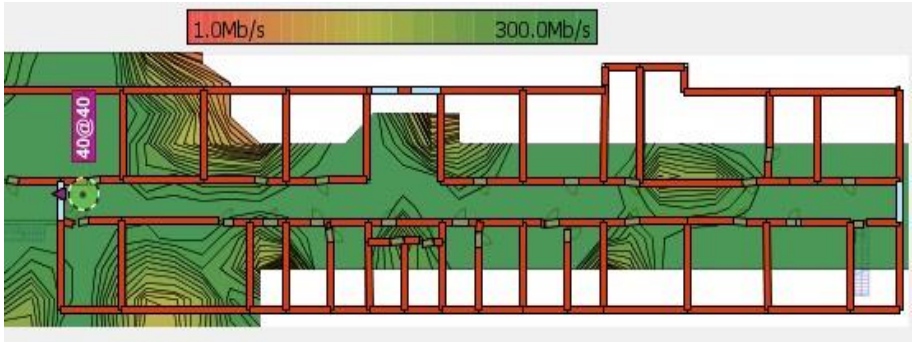

Figure 1. The simulated throughput in the 802.11n wireless network

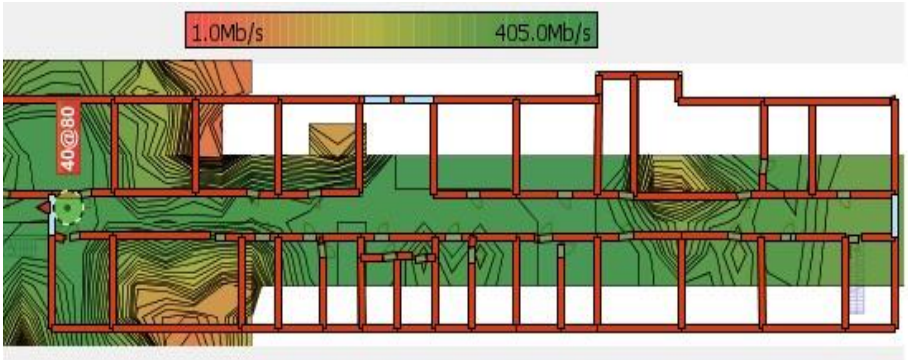

Figure 2. The simulated throughput in the 802.11ac wireless network

The average simulated throughput is 280 Mbps in LOS conditions (Fig. 1). The average simulated throughput is 150 Mbps in NLOS conditions, when the distance from access point to the user was 6 m. If the user is 40 m away from the AP (NLOS conditions), the average simulated throughput is 60 Mbps. The results from the 802.11ac throughput simulation (Fig.2) showed that the average throughput is 350 Mbps in LOS (Line of Sight) conditions. In this case, the distance from AP to the user was 1 m. Due to this the simulated throughput in the 802.11ac wireless network is 43% bigger than the throughput in the 802.11n network. As the user quite often uses Wi-Fi in NLOS conditions, the 802.11ac standard is more effective in this way also. The average throughput is 250 Mbps in NLOS (Non-Line of Sight) conditions, when the distance from access point to the user was 6 m, and 65 Mbps, when the distance was 40 m. That means the simulated throughput in 802.11ac network differences in 120 Mbps, when the distance is 6 m, and in 5 Mbps, when the distance is 40 m.

The signal strength is the most basic requirement for a wireless network, because low signal strength means unreliable connection and/or low data throughput. The

simulated signal strength in 802.11n and in 802.11ac wireless networks is presented in Figures 3 – 4.

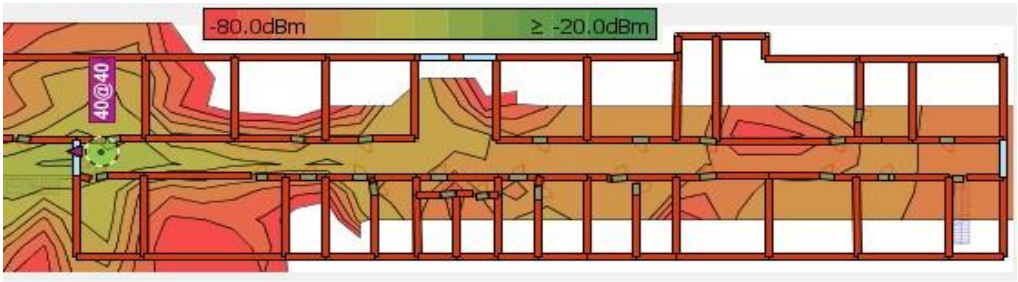

Figure 3. The simulated signal strength in the 802.11n wireless network

According to these results, it can be stated, that the signal strength in 802.11ac wireless network is more influenced by the obstacles (walls, partitions, etc.) than in 802.11n. This is because of the channel bandwidth, used in 802.11n [8].

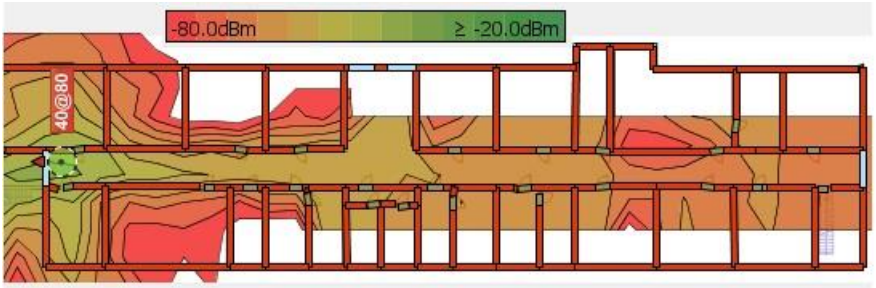

Figure 4. The simulated signal strength in the 802.11ac wireless network

Due to the results from the simulations, the 802.11ac wireless network provides 3 times faster connection than 802.11n, but its signal strength is more influenced by the obstacles.

3. EXPERIMENTAL INVESTIGATIONS FOR THE THROUGHPUT EVALUATION OVER IEEE 802.11N AND 802.11AC WIRELESS NETWORKS

After the simulations, it is necessary to investigate the parameters of the wireless networks based on 802.11n and 802.11ac standards. The experiments were carried out in the 4th floor of the building at Kaunas University of technology, Department of Telecommunications. Its layout corresponds to the scheme, used during the simulations. The structure of the experimental network and LOS/NLOS conditions is presented in Figure 5.

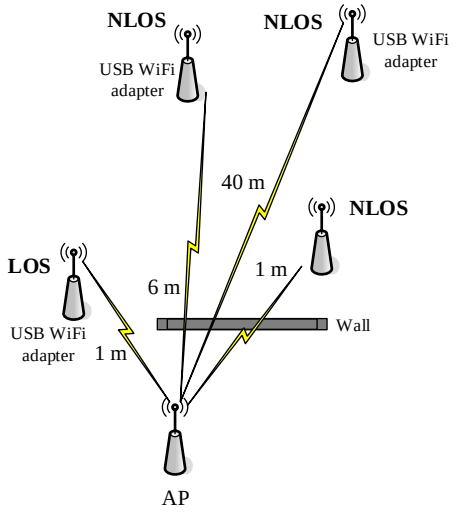

Figure 5. The structure of the experimental network and its LOS/NLOS conditions

The parameters, which were investigated: the throughput and the signal strength. The results of the investigated throughput of 802.11n and 802.11ac wireless networks in NLOS conditions are presented in Figures 6, 7.

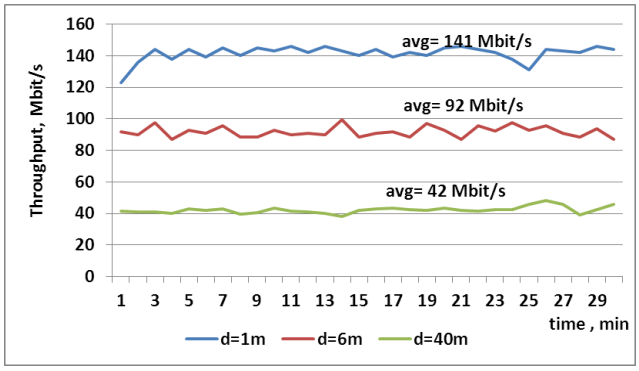

Figure 6. The investigated throughput of 802.11n wireless network in NLOS conditions

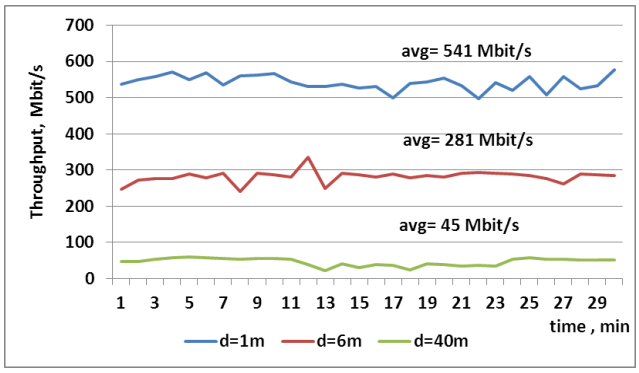

Figure 7. The investigated throughput of 802.11ac wireless network in NLOS conditions

According to the results of the investigated throughput in NLOS conditions, it can be seen, that the distance between the AP and the user influences the throughput of 802.11ac wireless network. In this case, the average throughput of 802.11ac wireless network is 281 Mbps in 6 m distance and only 45 Mbps in 40 m distance. The average throughput of 802.11n wireless network is only 7% less in the distance of 40 m from AP.

The results in Figure 8 show the ratio of the throughput between the different standards in accordance to the signal strength. The ratio of the investigated throughput between the different standards shows that the investigated throughput differences in ~ 4 times if the received signal strength indication (RSSI) is -65 dBm. In this case, the signal strength of 802.11n wireless network in NLOS conditions is more appropriate for the wireless connections.

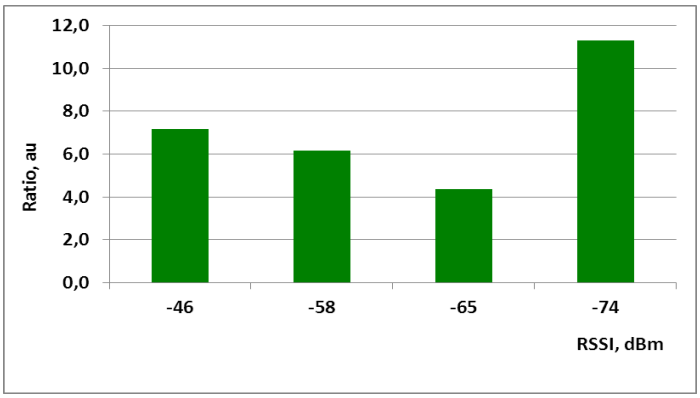

Figure 8. The ratio of the investigated throughput between the different standards

The investigated throughput of 802.11ac wireless network in LOS conditions is presented in Figure 9. Its comparison with the results from the simulations is presented also in this Figure. It can be seen, that the investigated 802.11ac wireless connection is 1.5 times faster than the simulated.

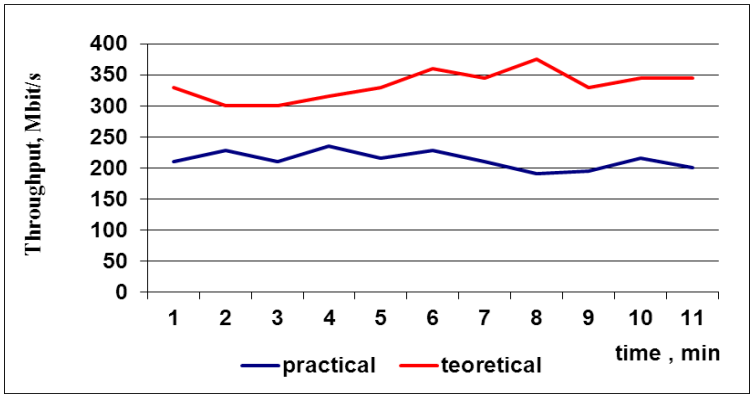

Figure 9. The comparison of 802.11ac throughput in LOS conditions

In order to evaluate the 802.11ac throughput in realistic conditions, it is necessary to investigate the impact of traffic load on it (Fig. 10).

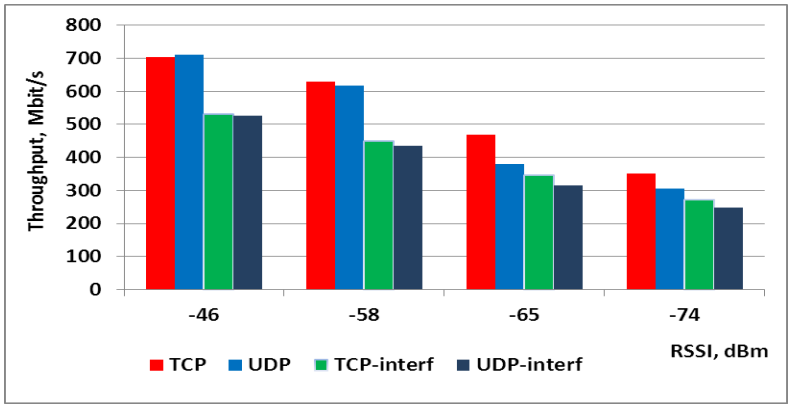

Figure 10. The influence of the traffic load to the 802.11ac throughput

According to the results in Figure 10, if the signal strength is falling and there are the additional loads in the network (TCP (*Transmission Control Protocol*), UDP (*User Datagram Protocol*) sessions) the throughput of 802.11ac wireless network can be reduced in 2 times. However, even the throughput can be reduced the wireless network of 802.11ac standard provides access to a faster Wi-Fi connection than 802.11n.

4. THE EXPERIMENTAL EVALUATION OF VOIP QOS OVER IEEE 802.11AC WIRELESS NETWORK

The broadcasting of Real-time services, such as VoIP, depends on the quality of the communication process over wireless connection and its continuity. The throughput, the packets' delay and loss, the signal level are the main QoS parameters for VoIP

service transmission over wireless network. Due to this, the experimental investigations were carried out in order to evaluate the QoS parameters of VoIP service transmission over 802.11ac wireless network. The structure of the experimental 802.11ac wireless network is presented in Figure 11.

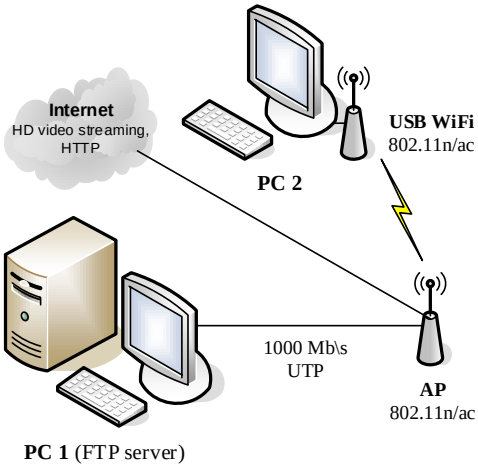

Figure 11. The structure of the experimental network

This experimental 802.11ac wireless network consists of two computers, both of them were working as a VoIP users, and the wireless access point (AP). The model of the access point was D-Link DIR 850L, which is working on 802.11n and 802.11ac standards. It has four MIMO antennas and dual band (2.4 GHz; 5 GHz) performance up to 1167 Mbps. The measurements were made using *Jperf 2.0.2v*, *InSSIDer*, *SJ Phone*, *Wireshark 1.12.0 Network Analyzer* software. G.711 voice codec was used for VoIP service transmission. The distance from AP to the user was 1 m. The experimental investigations have been carried out for three different scenarios. At first, only VoIP calls were made in the experimental 802.11ac network without any additional traffic in the network. The results for the delay and the jitter of VoIP service transmission over IEEE 802.11ac wireless network are presented in Figure 12 and Figure 13. According to the results in these Figures, it can be stated, that Voice over IP transmission in 802.11ac wireless network is performed with a high quality, if there is no any additional traffic in the network. The average delay of VoIP packets was 45.56 ms and the average jitter – 13.44 ms, the loss of VoIP packets – 0 %.

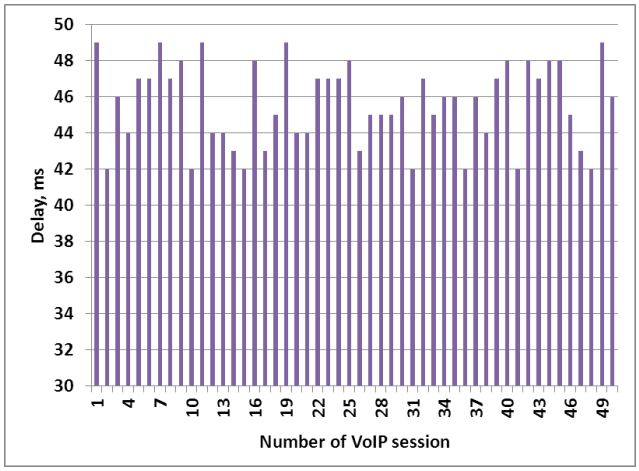

Figure 12. The delay of VoIP packets transmission over 802.11ac network

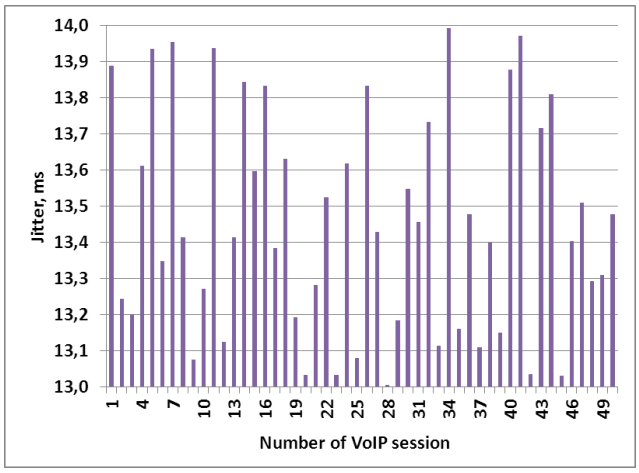

Figure 13. The jitter of VoIP packets transmission over 802.11ac network

The transmission of VoIP service with the additional traffic over the 802.11ac network was done during the second and the third scenarios. The additional traffic (for the second scenario) was created from the HD (High Definition) video and FTP (File Transfer Protocol) transmissions to the VoIP user (PC2 in Figure 11) at the same time, when VoIP calls were made. The results of the QoS parameters for VoIP service during the second scenario are presented in Figures 14 - 16.

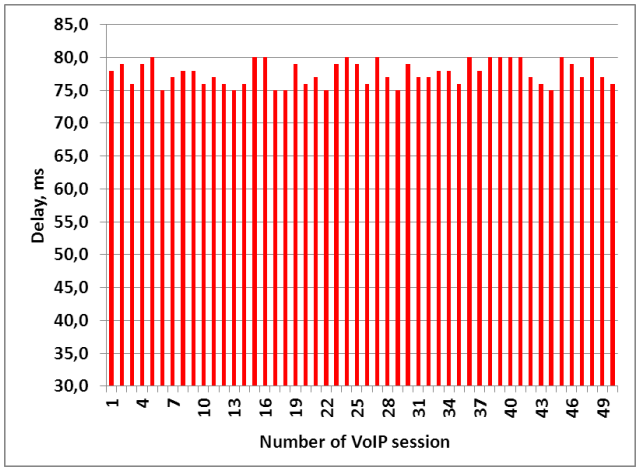

Figure 14. The delay of VoIP packets transmission with the additional video/FTP traffic over 802.11ac network

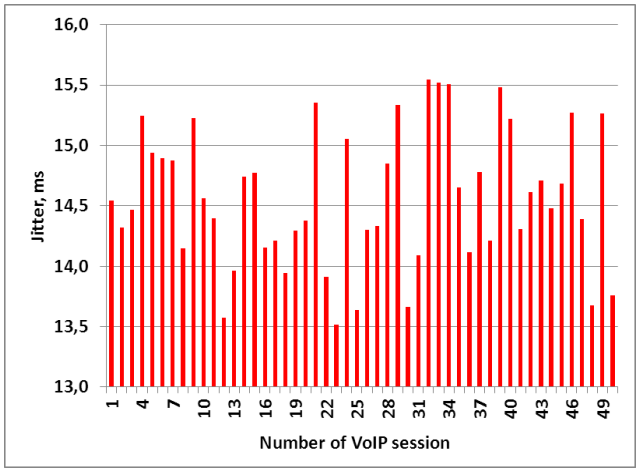

Figure 15. The jitter of VoIP packets transmission with the additional video/FTP traffic over 802.11ac network

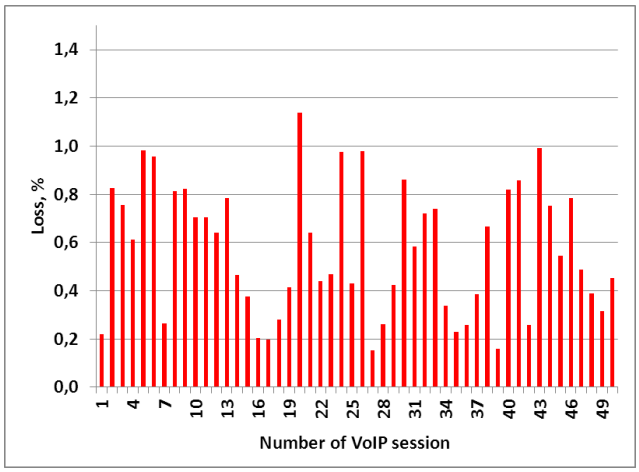

Figure 16. The loss of VoIP packets transmission with the additional video/FTP traffic over 802.11ac network

The results of the investigations during the second scenario showed, that the additional traffic over 802.11ac wireless network influences the quality of VoIP service. However, such influence was observed only to minor changes in the voice calls, which the user felt as a voice jerking. In this case the average delay of VoIP packets was 77.6 ms and the average jitter – 14.7 ms. The loss of VoIP packets was 0.7 %.

The additional traffic from the HD video, FTP and HTTP (Hyper Text Transfer Protocol) transmissions was created to the VoIP user at the same time, when VoIP calls were made during the third scenario. The results of these investigations are presented in Figures 17 – 19.

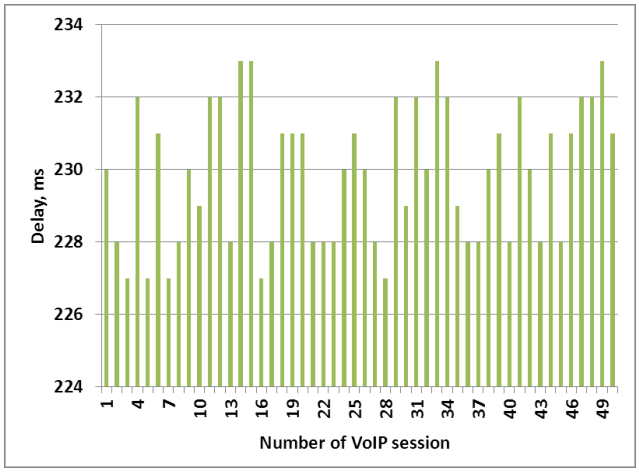

Figure 17. The delay of VoIP packets transmission with the additional video/FTP/HTTP traffic over 802.11ac network

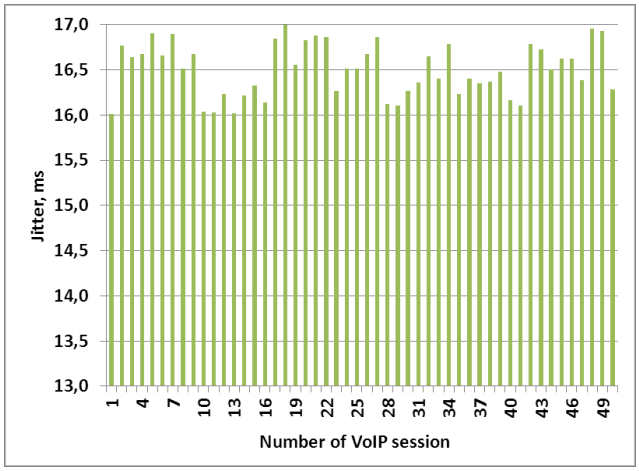

Figure 18. The jitter of VoIP packets transmission with the additional video/FTP/HTTP traffic over 802.11ac network

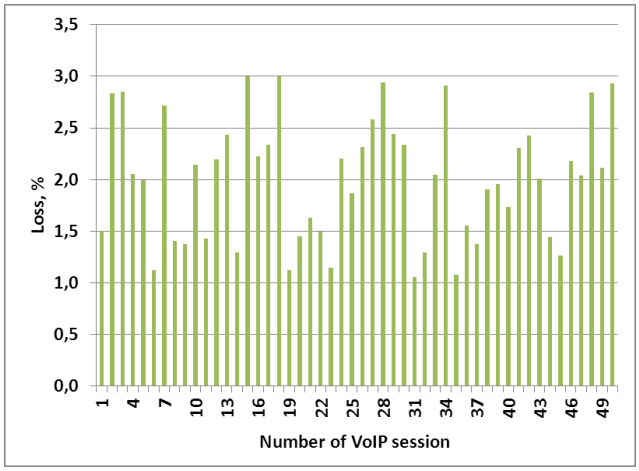

Figure 19. The loss of VoIP packets transmission with the additional video/FTP/HTTP traffic over 802.11ac network

As it seen from the results in Figures 17–19, the transmission of VoIP service is affected by the additional video/FTP/HTTP traffic, because the average loss of VoIP packets is 2 %. Such loss of VoIP packets value exceeds the recommended limit of 1 % accord to the ITU-T G.711 recommendation. The average delay of VoIP packets was 229 ms and the average jitter – 16.23 ms. In this way, the user felt many negative things, like voice jerking or echo, however the transmission of VoIP service was not braked.

So generally, the IEEE 802.11ac standard allows the transmission of VoIP service over the wireless network.

5. THE SIMULATION OF VOIP QOS OVER IEEE 802.11N (5 GHZ) WIRELESS NETWORK

The simulation of 802.11n wireless network was carried out in order to evaluate the QoS parameters of VoIP service transmission over 5 GHz frequency range. The structure of the simulated 802.11n wireless network was the same as the experimental network (Figure 11). Riverbed Modeler Academic Edition 17.5 software was used for the simulation.

The simulation has been carried out for three different scenarios. At first scenario only VoIP calls were made without any additional traffic in the simulated 802.11n network. The transmission of VoIP service with the additional traffic over the 802.11n network was done during the second and the third scenarios. The additional traffic (for the second scenario) was created from the HD (High Definition) video and FTP (File

Transfer Protocol) transmissions to the VoIP user (PC2 in Figure 11) at the same time, when VoIP calls were made. The additional traffic from the HD video, FTP and HTTP (Hyper Text Transfer Protocol) transmissions was created to the VoIP user at the same time, when VoIP calls were made during the third scenario.

The results for the delay, MOS (Mean Opinion Score) and Loss of VoIP service transmission over IEEE 802.11n wireless network are presented in Figure 20, Figure 21 and Figure 22. The results of the QoS parameters for VoIP service during the second and the third scenarios are presented in these Figures also.

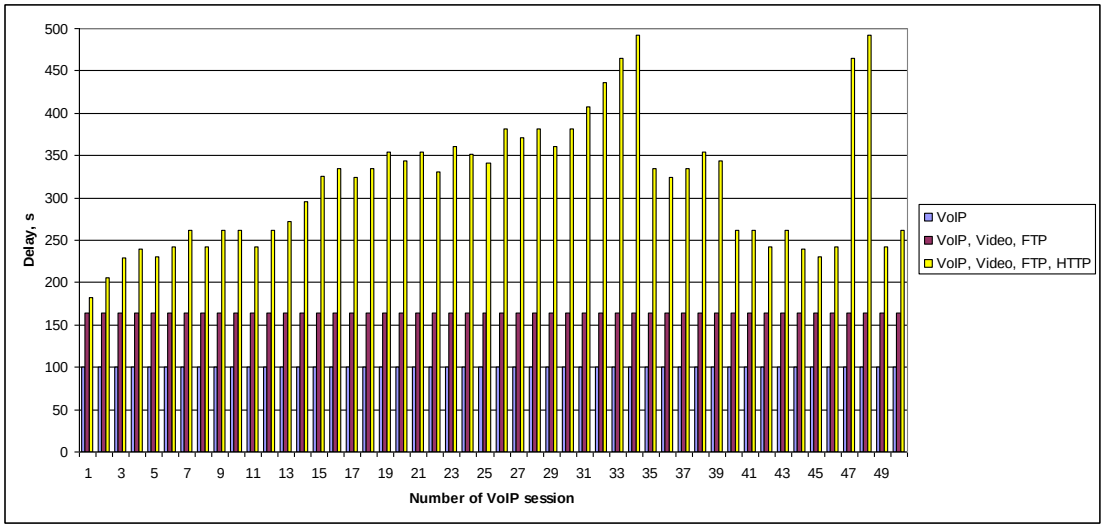

Figure 20. The delay of VoIP packets transmission over 802.11n network without/ with the additional video/FTP/HTTP traffic

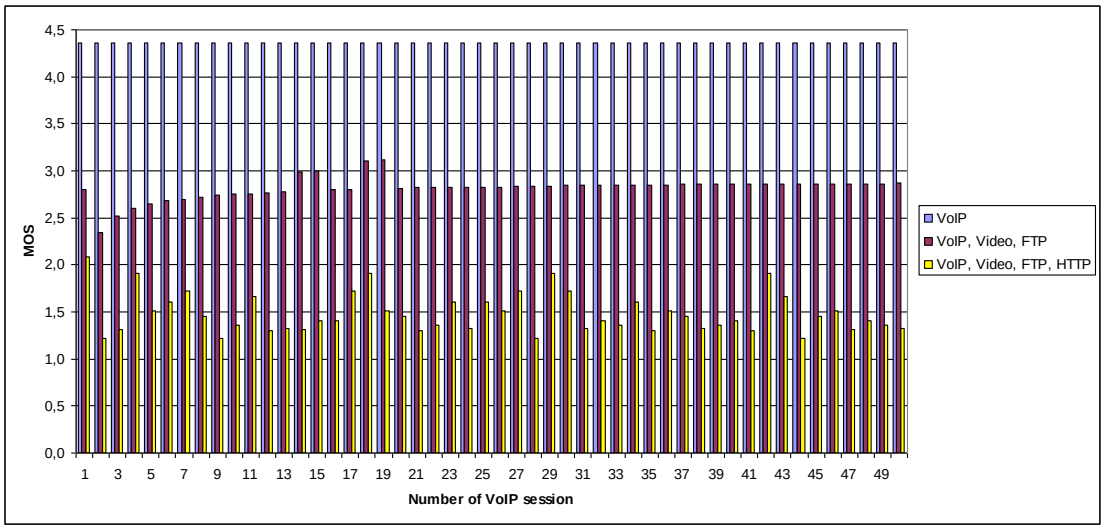

Figure 21. The MOS of VoIP packets transmission over 802.11n network without/ with the additional video/FTP/HTTP traffic

According to the results of all these investigations, it can be stated, that Voice over IP transmission in 802.11n wireless network is performed with a high quality, if there is no any additional traffic in the network. The delay of VoIP packets is about twice bigger (100 ms) than in the case of 802.11ac wireless network, but average value of MOS parameter is 4.36 and average of packets loss is 0.3 %.

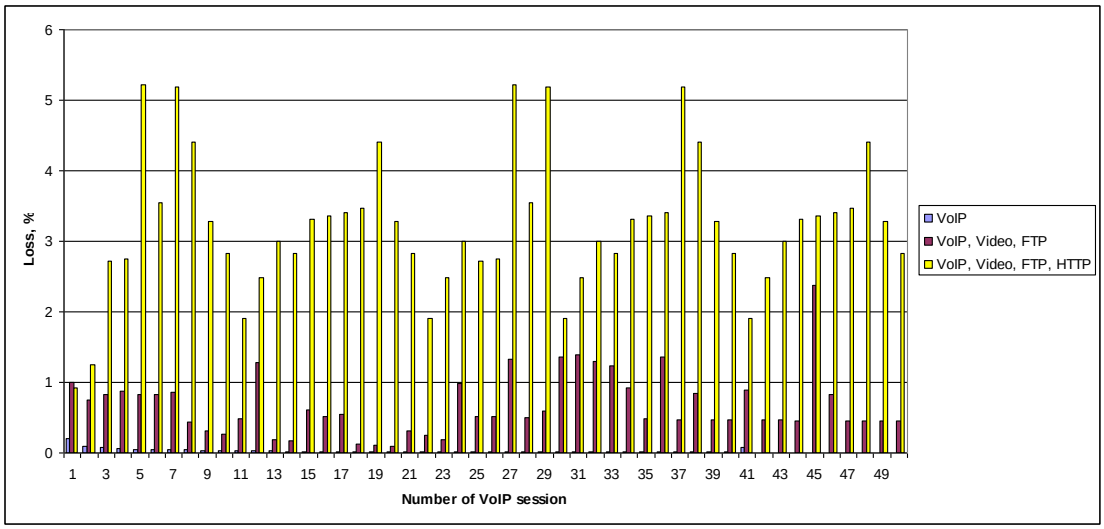

Figure 22. The loss of VoIP packets transmission over 802.11n network without/ with the additional video/FTP/HTTP traffic

The results of the simulation during the second scenario showed, that the additional traffic over 802.11n wireless network influences the quality of VoIP service and such influence is much higher than in the case of 802.11ac wireless network. So the authors observed a high decrease in the QoS of the voice calls. In this case the average delay of VoIP packets was 164 ms and the average MOS value only 2.8. The loss of VoIP packets was 0.68 %.

As it seen from the results in Figures 20–22, the transmission of VoIP service is affected by the additional video/FTP/HTTP traffic, because the average loss of VoIP packets is 3.2 %. Such loss of VoIP packets value exceeds the recommended limit of 1 % accord to the ITU-T G.711 recommendation. The average delay of VoIP packets was 315 ms and the MOS value was extremely low – only 1.5. In this way, the user felt many negative things, like voice jerking or echo, however the transmission of VoIP service was not broken.

So generally, the IEEE 802.11ac standard is more progressive and better adapted to allow the transmission of VoIP service with higher quality of service over the wireless network with high background load.

5. CONCLUSIONS

In this paper, the authors investigated the IEEE 802.11ac wireless network and compared it with IEEE 802.11n. According to the obtained results, it can be stated, that the 802.11ac wireless network provides 3 times faster connection than 802.11n, but its signal strength is more influenced by the obstacles.

The investigation of MOS value for the VoIP service in the 802.11n wireless network showed that the additional traffic as HD video, FTP and HTTP decreases this value from 4.36 (without additional traffic) until 1.5.

The investigation of the VoIP QoS over 802.11n and 802.11ac wireless networks showed that VoIP transmission is performed with a high quality, if there is no additional traffic in the network. The additional traffic in the 802.11ac network influences the average loss in 2 % and in the 802.11n network in 3.2 % for VoIP packets.

REFERENCES

[1] Eng Hwee Ong, Jarkko Kneckt, Olli Alanen, Zheng Chang, Toni Huovinen and Timo Nihtila. "IEEE 802.11ac: Enhancements for Very High Throughput WLANs Personal Indoor and Mobile Radio Communications (PIMRC)", *in Proceedings of IEEE 22nd International Symposium*, 2011, pp. 849 – 853.

[2] Lochan Verma, Mohammad Fakharzadeh and Unghyun Choi. "WiFi on Steroids: 802.11ac and 802.11ad", *IEEE Wireless Communications*, Vol. 20, No. 6, 2013, pp. 30 – 35.

[3] Emna Charfi, Lamia Chaari, and Lotfi Kamoun. "PHY/MAC Enhancements and QoS Mechanisms for Very High Throughput WLANs: A Survey", *IEEE Communications Surveys & Tutorials*, Vol. 15, No. 4, 2013, pp. 1714 – 1735.

[4] Ali A. Khavasi; Mojtaba Aajami; Hae-Ryeon Park; Jung-Bong Suk. "Video transmission over IEEE 802.11ac downlink multi-user: max-min fair link adaptation strategy", *Electronics Letters*, Vol. 50, No. 12, 2014, pp. 898 – 900.

[5] Oscar Bejarano, Edward W. Knightly and Minyoung Park. "IEEE 802.11ac: From Channelization to Multi-User MIMO", *IEEE Communications Magazine*, Vol: 51, No. 10, 2013, pp. 84 – 90.

[6] Yu H., Kim T. "Beamforming transmission in IEEE 802.11ac under time-varying channels", *the scientific world journal*, Vol. 2014, 2014, pp. 920 – 937.

[7] Brūzgienė, Rasa; Narbutaitė, Lina; Adomkus, Tomas; Cibulskis, Romualdas. "The impact of video streaming on quality of experience over 802.11n dual Band networks: experimental evaluation", *Electronics and electrical engineering*, Vol. 20, no. 6, 2014, p. 158-161.

[8] F. Heereman, W. Joseph, E. Tanghe, D. Plets and L. Martens. "Prediction of Range, Power Consumption and Throughput for IEEE 802.11n in Large Conference Rooms Antennas and Propagation (EUCAP)", *in Proceedings of the 5th European Conference*, April 2011, pp. 692 – 696.

GENERAL SPATIAL CORRELATION MODEL IN VON MISES ANGLE OF ARRIVAL DISTRIBUTION ENVIRONMENT

S. V. Savov*, M. H. A. J. Herben**

* Department of Electrical Engineering
Technical University of Varna,
9010 Varna, Bulgaria
e-mail: sava.savov12@gmail.com

** Department of Electrical Engineering
Eindhoven University of Technology,
5600 MB Eindhoven, The Netherlands

Abstract

Analytical expressions are derived for the envelope correlation of the signals measured with two closely spaced antennas in an urban multipath environment. The angles-of-arrival (AoA) of the multipath waves are assumed to be von Mises distributed. It are closed-form expressions and therefore easier to implement in for instance MIMO-capacity calculations than previously published formulas that include infinite summations. Moreover, the new expressions are not restricted to an array of isotropic radiators but also hold for an array of dipole antennas.

1. INTRODUCTION

In mobile communication systems multiple waves are propagating between transmitter and receiver. This multipath propagation is caused by electromagnetic wave reflection, diffraction and scattering and transmission through objects like buildings, trees, etc. [1-3]. All these waves arrive at the receiver with different angle-of-arrival (AoA) [4].

For next generation 4G radio systems (using e.g. smart antennas or MIMO) this angular dispersion of radiowaves is becoming increasingly important. In beamforming systems it strongly influences the effect of nulling out interference or directing a beam to obtain a maximum signal level. In MIMO systems the angular dispersion has a major effect on capacity and diversity gain [5-7]. This is because angular dispersion results in a decorrelation of the radio signals at the MIMO antenna elements. A larger angular spread gives a lower signal correlation leading to an increase of MIMO system capacity.

There are two approaches to calculate the signal correlation: 1) based on antenna pattern [8-11]; 2) based on S-parameters [12-13]. In the present paper the first mentioned approach will be used.

If the AoA-distribution is uniform in azimuth the correlation of the envelope signals received at two closely spaced antenna elements is given by a zeroth-order Bessel function of the first kind. This scenario was first considered and analyzed by Clarke [14] and also described in the classic book of Jakes [15]. Because the uniform AoA-distribution does not generally hold, later on various papers appeared that considered other probability density functions (pdf) of AoA, such as Gaussian and von Mises. The von Mises pdf is best suited for AoA because it is a *continuous periodical pdf*.

In a recent paper by Queiroz et al. expressions were derived for the signal correlation assuming the von Mises pdf [16]. These expressions include infinite summations that must be

truncated in order to obtain numerical results. Furthermore, the radiation patterns of the antenna elements are assumed to be *omnidirectional*.

In the present paper closed-form analytical expressions of the envelope correlation that only consist of simple Bessel functions are derived and we will extend these easy-to-implement expressions to the case of *short dipole antenna elements*. These results are novel (to the authors knowledge). Section II deals with the correlation functions in case of small isotropic sources and in section III the obtained analytical results are extended to the case of two similar broadside short dipoles. Numerical results for both cases are given in Section IV. The paper will be concluded with a physical explanation of the obtained results in section V.

2. CALCULATION OF ENVELOPE CORRELATIONS FOR TWO SIMILAR ISOTROPIC ANTENNAS

The geometry of the problem is shown in Fig.1. The probability function (pdf) of the random variable ϕ, that is an angle-of-arrival AoA) of a multipath wave, is assumed to be given by the "*von Mises model*"

$$p_{\kappa}^{\phi_p}(\phi) = \frac{1}{2\pi I_0(\kappa)} e^{\kappa \cos(\phi - \phi_p)} \tag{1}$$

where κ is a *distribution parameter*, ϕ_p is the *mean AoA*, and $I_0(\kappa)$ is a modified Bessel function of the first kind and zero order. Small values of the angular spread parameter (κ) are related to a large angular spread of the multipath waves, while large values of this parameter are related to a small angular spread around ϕ_p .

The pdf (1) satisfies the following normalization condition

$$\int_{-\pi}^{\pi} p_{\kappa}^{\phi_p}(\phi) d\phi = 1 \tag{2}$$

The spatial correlation between the signals received with two similar isotropic antennas separated by distance (d) and positioned on the x-axis (Fig.1) is given by the following integral [6]

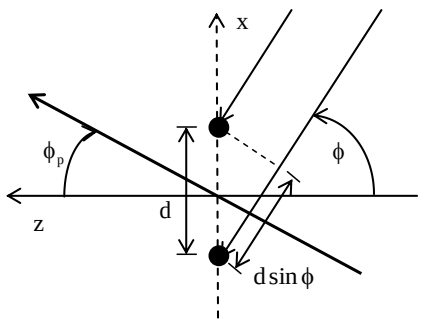

Figure 1. Two similar isotropic sources.

$$\rho_{\kappa}^{\phi_p}(\xi) = \frac{\int_{-\pi+\phi_p}^{\pi+\phi_p} e^{j\xi\sin\phi} e^{\kappa\cos(\phi-\phi_p)} d\phi}{2\pi I_0(\kappa)} \tag{3}$$

and here for convenience the *relative distance parameter* ($\xi = 2\pi d/\lambda$) is introduced.

The more often used envelope correlation ρ_e is related with this correlation by the following equation

$$\rho_e(\xi) = |\rho(\xi)|^2 \tag{4}$$

Note: in our further investigation the dependence of this functions on other parameters (κ, ϕ_p) will be assumed but omitted for convenience, and only the dependence on the variable (ξ) will be indicated explicitly.

Now we will make some simple transformations in the exponential term in the integrant of (3). Rewriting this term as

$$e^{S(\xi)\cos(\phi-\theta(\xi))} \tag{5}$$

where after elementary trigonometric transformations

$$\begin{aligned} \kappa\cos\phi_p &= S(\xi)\cos\theta(\xi), \\ \kappa\sin\phi_p + j\xi &= S(\xi)\sin\theta(\xi) \end{aligned} \tag{6}$$

the following explicit expressions for the new complex variables ($S(\xi),\ \theta(\xi)$) are obtained

$$\begin{aligned} S(\xi) &= \sqrt{\kappa^2 - \xi^2 + j2\kappa\xi\sin\phi_p}, \\ \theta(\xi) &= \tan^{-1}\left[\frac{\kappa\sin\phi_p + j\xi}{\kappa\cos\phi_p}\right] \end{aligned} \tag{7}$$

It is easy to be checked that the limiting case ($d \to 0$) yields to $S(0) = \kappa,\ \ \theta(0) = \phi_p$ (an expected result).

Using an integral representation of the modified Bessel function of the second kind and the order zero $I_0(\ .\ )$ [17]

$$\int_{-\pi}^{\pi} e^{\kappa\cos(\zeta)} d\zeta = 2\pi I_0(\kappa) \tag{8}$$

(here $\phi - \phi_p = \zeta$ is assumed) the following result for the spatial correlation function is obtained

$$\rho_{\kappa}^{\phi_p}(\xi) = \frac{I_0(S(\xi))}{I_0(\kappa)} \tag{9}$$

Then the envelope correlation can be easy obtained by equation (4).

This is a very compact and general result for the correlation function. In Appendix A it is shown that this result is completely *equivalent* to the result in [16], obtained in terms of

complicated Bessel-trigonometric infinite series. The advantage of our expression (9) in comparison with the one presented in [16] is that ours is much *more concise* and therefore easier to implement in for instance MIMO-capacity analysis software.

Some numerical results will be shown in section IV of the envelope correlation for a couple of isotropic sources as a function of antenna spacing with the mean AoA (ϕ_p) and angular spread parameter (κ) as parameters.

3. CALCULATION OF ENVELOPE CORRELATIONS FOR TWO SIMILAR SHORT DIPOLES

Here only the broadside case is considered, because then the mutual coupling between the antenna elements is smallest, which is needed for MIMO antenna systems. In that case the dipole current is flowing along the array (x-axis), as shown in Fig.2, resulting in an eight shaped radiation pattern in the (x-z) plane with nulls towards adjacent antenna elements. Analysis of the end-fire dipole case can be performed in the same way and in the correlation function the same two special functions (modified Bessel functions of order zero and one) can be introduced.

The general expression for two similar short dipoles at a distance (d) from each other situated in the azimuth plane (ϕ) is given by the following integral [6]

$$\rho_{\kappa}^{\phi_p}(\xi) = \frac{\int_{-\pi+\phi_p}^{\pi+\phi_p} F^2(\phi) e^{j\xi\sin\phi} e^{\kappa\cos(\phi-\phi_p)} d\phi}{\int_{-\pi+\phi_p}^{\pi+\phi_p} F^2(\phi) e^{\kappa\cos(\phi-\phi_p)} d\phi} \equiv \frac{N(\xi)}{D(\kappa)} \tag{10}$$

where $N(\xi)$ is the numerator, $D(\kappa)$ is the denominator, and $F^2(\phi) = \cos^2\phi$ is the power radiation pattern of the dipole.

The auxiliary function $S(\xi)$ is defined in (7). It is easy to see that the variable in the denominator can be obtained from the numerator by simply letting $\kappa = S(0)$. After using equations (6) and (7) we come to the following expression for the numerator

$$N(\xi) = \int_{-\pi+\phi_p}^{\pi+\phi_p} \cos^2\phi e^{S(\xi)\cos(\phi-\theta(\xi))} d\phi \tag{11}$$

After setting $\phi - \phi_p = \sigma$, the integral above can be rewritten in the following form

$$N(\xi) = \int_{-\pi}^{\pi} \cos^2(\sigma+\phi_p) e^{S(\xi)\cos(\sigma+\phi_p-\theta)} d\sigma \tag{12}$$

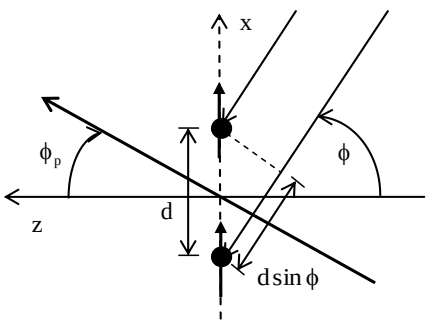

Figure 2. Two similar parallel short dipoles (broadside case).

and with the substitution $\sigma - \theta = \tau$ the integral becomes

$$N(\xi) = \int_{-\pi-\theta}^{\pi-\theta} \cos^2(\tau + \phi_p + \theta) e^{S(\xi)\cos(\tau+\phi_p)} d\tau \tag{13}$$

and with $\tau + \phi_p = \rho$ the integral can be written as

$$N(\xi) = \int_{-\pi+\psi}^{\pi+\psi} \cos^2(\rho + \theta) e^{S(\xi)\cos(\rho)} d\rho \tag{14}$$

where $\phi_p - \theta = \psi$ is assumed. Next, some transformations are performed in order to, at the end, arrive at closed form expression without integrals. It is well known that

$$\cos(\rho + \theta) = \cos\rho\cos\theta - \sin\rho\sin\theta \tag{15}$$

That yields to

$$N(\xi) = \int_{-\pi+\psi}^{\pi+\psi} \begin{bmatrix} \cos^2\rho\cos^2\theta + \sin^2\rho\sin^2\theta + \\ 2\sin\rho\cos\rho\sin\theta\cos\theta \end{bmatrix} e^{S(\xi)\cos(\rho)} d\rho \tag{16}$$

In the first integral $\cos^2\rho = 1 - \sin^2\rho$ is set and then it is combined with the second integral. Due to symmetry the third integral is equal to zero. The two remaining integrals take the form

$$N(\xi) = \cos^2\theta \int_{-\pi+\psi}^{\pi+\psi} (1 - \sin^2\rho) e^{S(\xi)\cos(\rho)} d\rho + \sin^2\theta \int_{-\pi+\psi}^{\pi+\psi} \sin^2\rho e^{S(\xi)\cos(\rho)} d\rho$$

That can be rearranged as follows

$$N(\xi) = \cos^2\theta \int_{-\pi+\psi}^{\pi+\psi} e^{S(\xi)\cos(\rho)} d\rho + \left(\sin^2\theta - \cos^2\theta\right) \int_{-\pi+\psi}^{\pi+\psi} \sin^2\rho e^{S(\xi)\cos(\rho)} d\rho \tag{17}$$

Here ψ is an arbitrary constant angle, that can be set to zero. Now we recognize in (17) the standard integral [17]

$$\int_{-\pi}^{\pi} \sin^{2m}\rho e^{\kappa\cos(\rho)} d\rho = 2\pi \frac{I_m(\kappa)}{\kappa^m} \quad (m = 0,\ 1) \tag{18}$$

which result is an extension of (8).

From (10) it is obvious that the denominator is related to the numerator for the particular value: $D(\kappa) = N(S(\xi = 0))$.

Applying (6) and excluding ($\sin\theta$, $\cos\theta$) that yields for the numerator the following final expression

$$N(\xi) = \frac{2\pi}{S^2(\xi)} \left\{ \kappa^2 \cos^2\phi_p I_0(S(\xi)) + \left[S^2(\xi) - 2\kappa^2\cos^2\phi_p\right] \frac{I_1(S(\xi))}{S(\xi)} \right\} \tag{19}$$

It is easy now to obtain a suitable expression for the denominator D(κ)

$$D(\kappa) = 2\pi\left\{\cos^2\phi_p I_0(\kappa) + \left[1 - 2\cos^2\phi_p\right]\frac{I_1(\kappa)}{\kappa}\right\} \tag{20}$$

After substitution of the equations (19) and (20) into (10) we come to the final expression of the spatial correlation coefficient $\rho(\xi)$. Applying (4) and taking a square of the absolute value yields the final expression for the envelope correlation $\rho_e(\xi)$.

4. NUMERICAL RESULTS

Here several numerical results of the envelope correlation function for a couple of similar small EM sources are presented. These results will be analysed and discussed in Section V. For comparison reasons, the same numerical values of the parameters ϕ_p and κ were used to compute the envelope correlations in case of isotropic sources and the broadside short dipoles.

4.1. case ($\phi_p = 0$).

1) <u>isotropic sources</u>

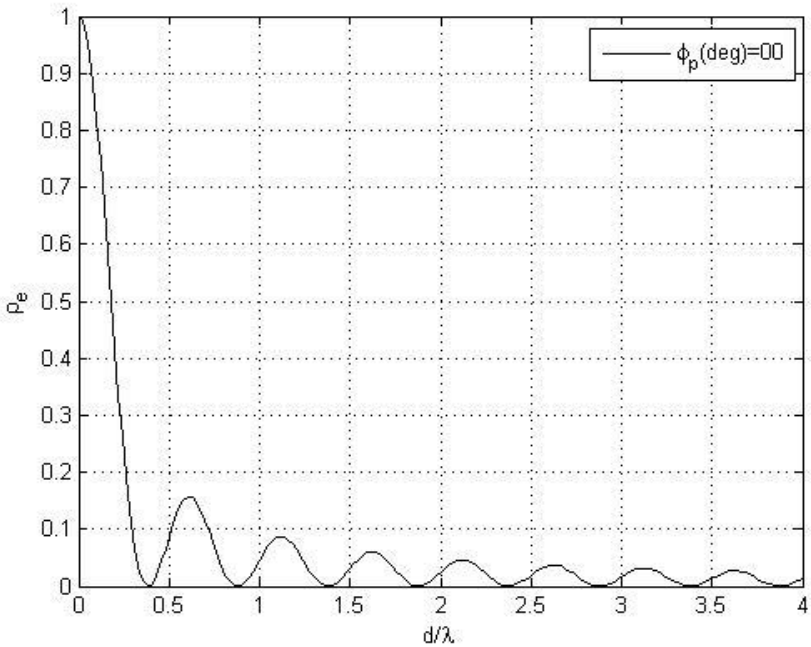

(a) ($\kappa = 0.25$)

2) broadside dipoles

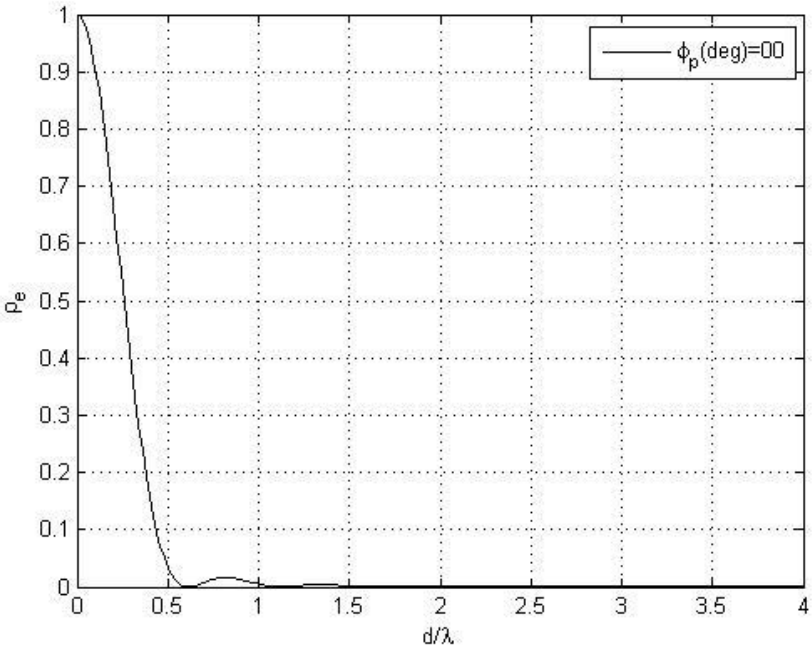

(a) ($\kappa = 0.25$)

1) isotropic sources

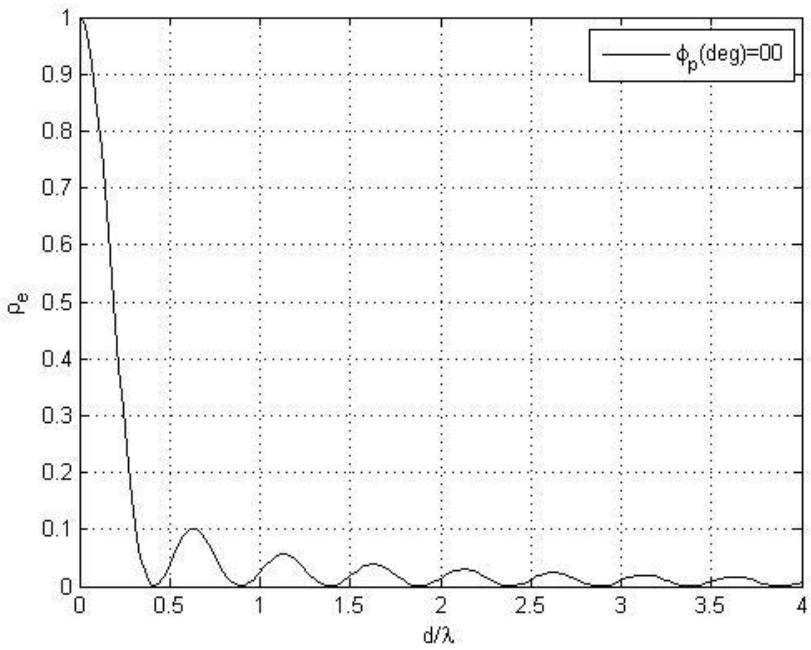

(b) ($\kappa = 1.0$)

2) broadside dipoles

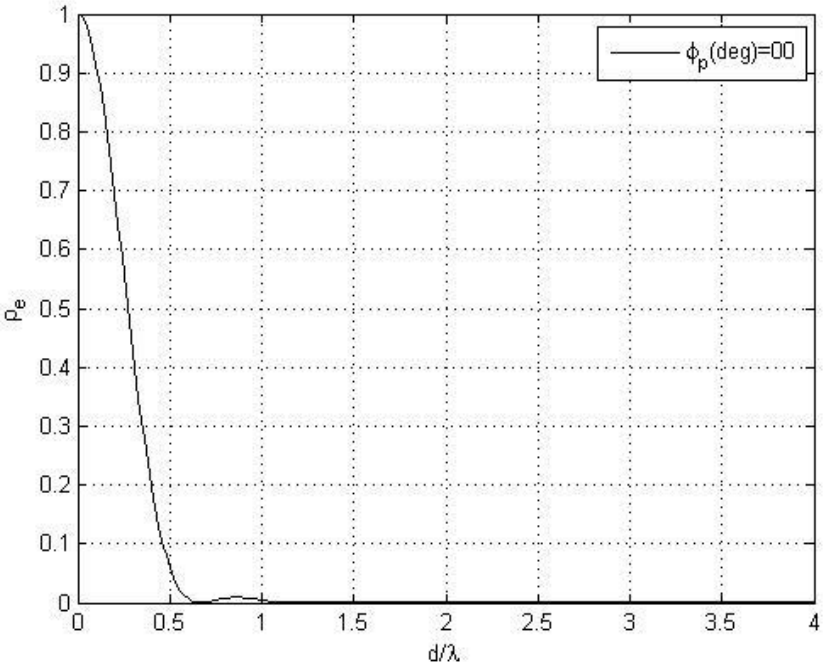

(b) ($\kappa = 1.0$)

1) isotropic sources

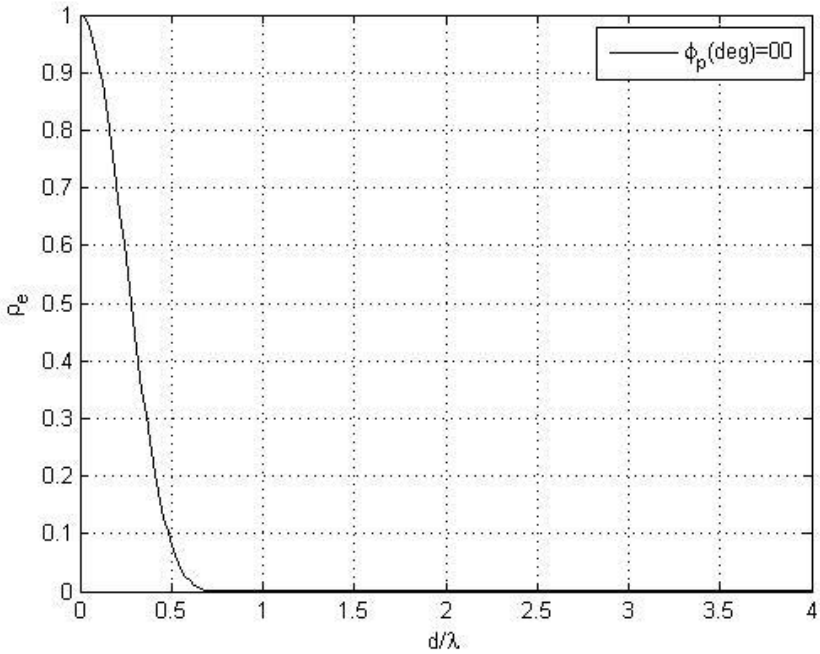

(c) ($\kappa = 4.0$)

2) broadside dipoles

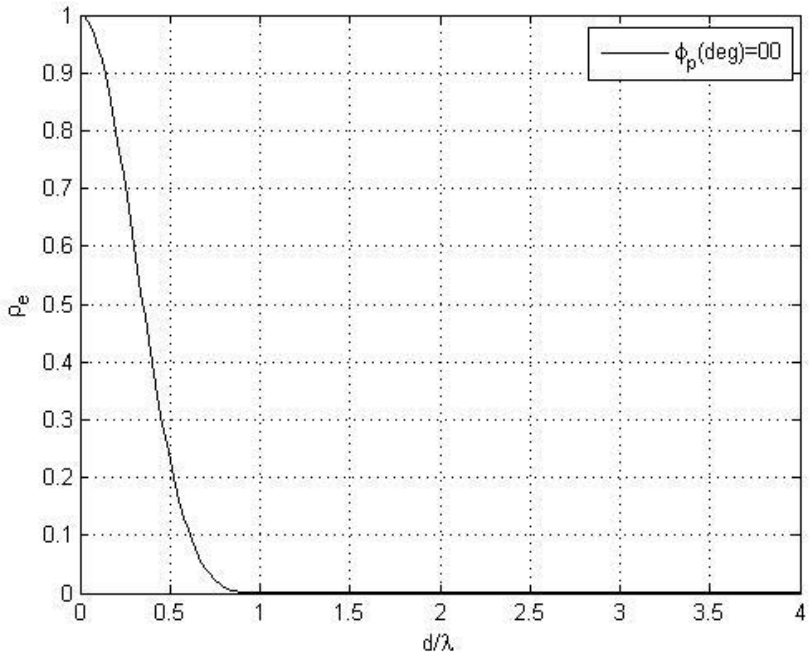

(c) ($\kappa = 4.0$)

Figure 3. Correlations for the case $\phi_p = 0$

4.2. case ($\phi_p = 45^0$)

1) isotropic sources

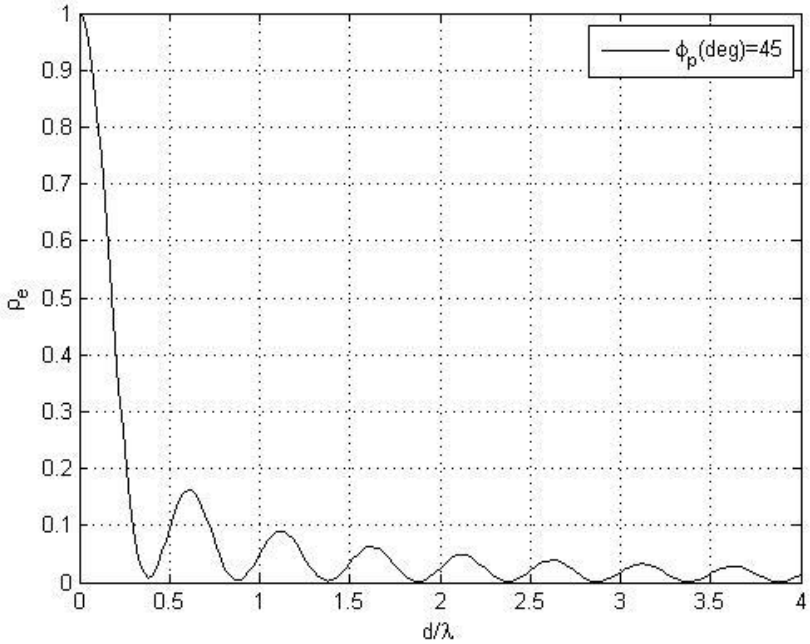

(a) ($\kappa = 0.25$)

2) broadside dipoles

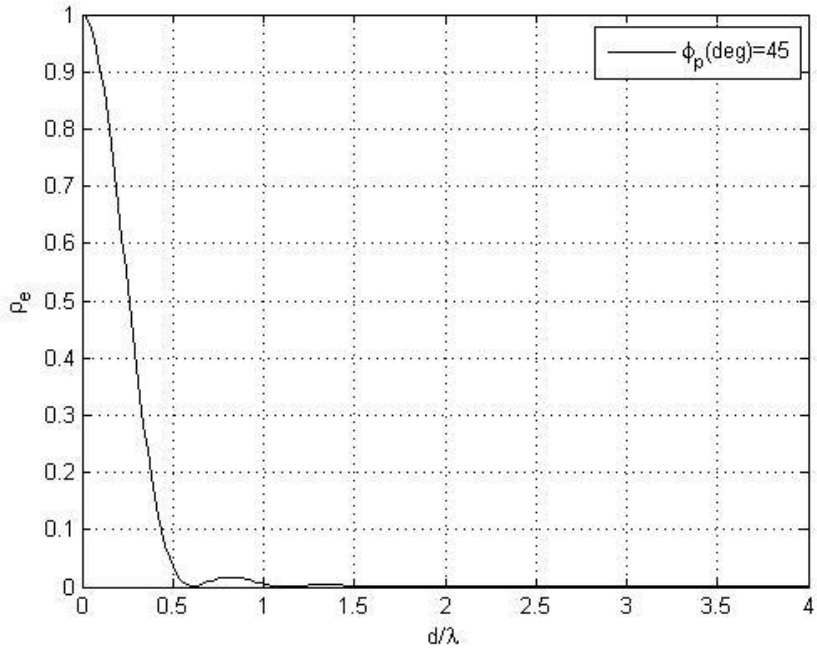

(a) ($\kappa = 0.25$)

1) isotropic sources

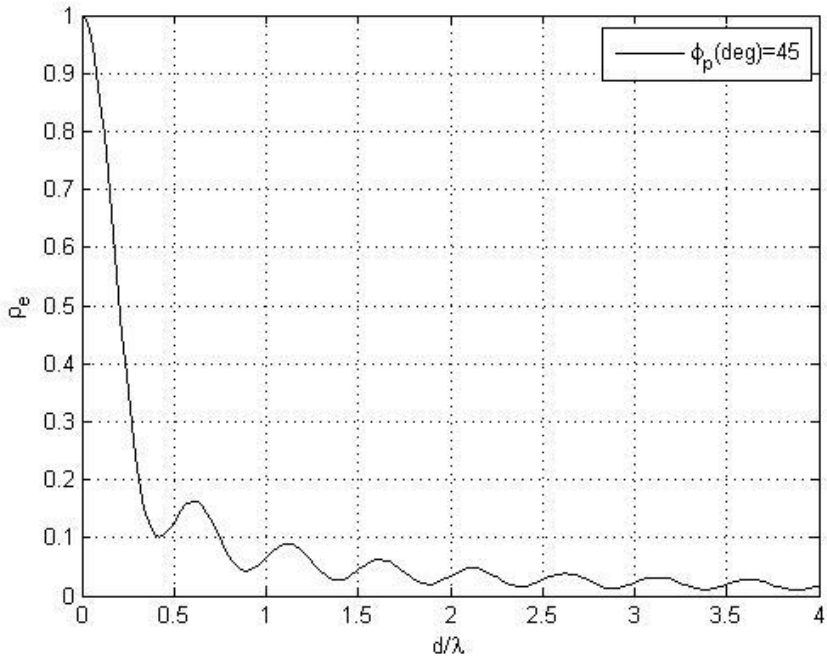

(b) ($\kappa = 1.0$)

2) broadside dipoles

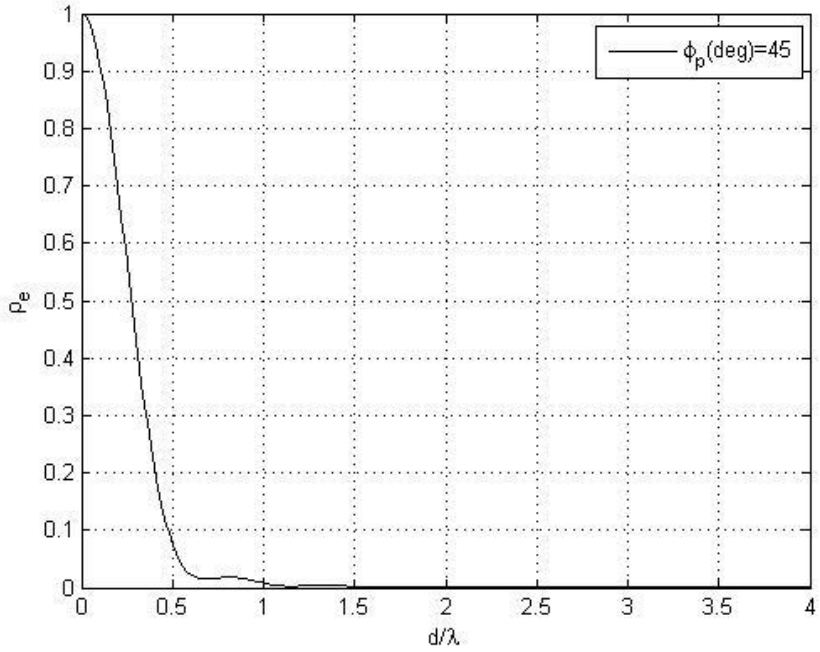

(b) ($\kappa = 1.0$)

1) isotropic sources

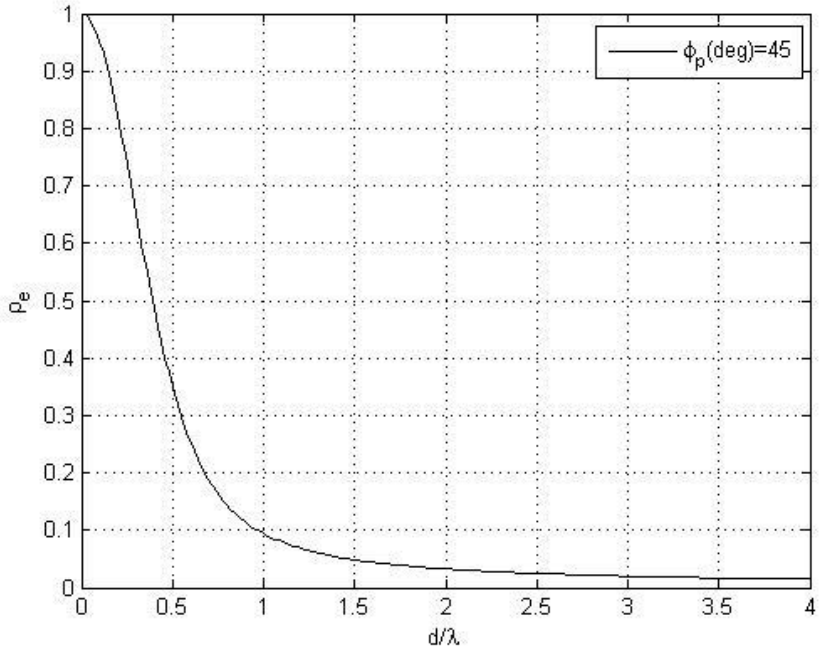

(c) ($\kappa = 4.0$)

2) broadside dipoles

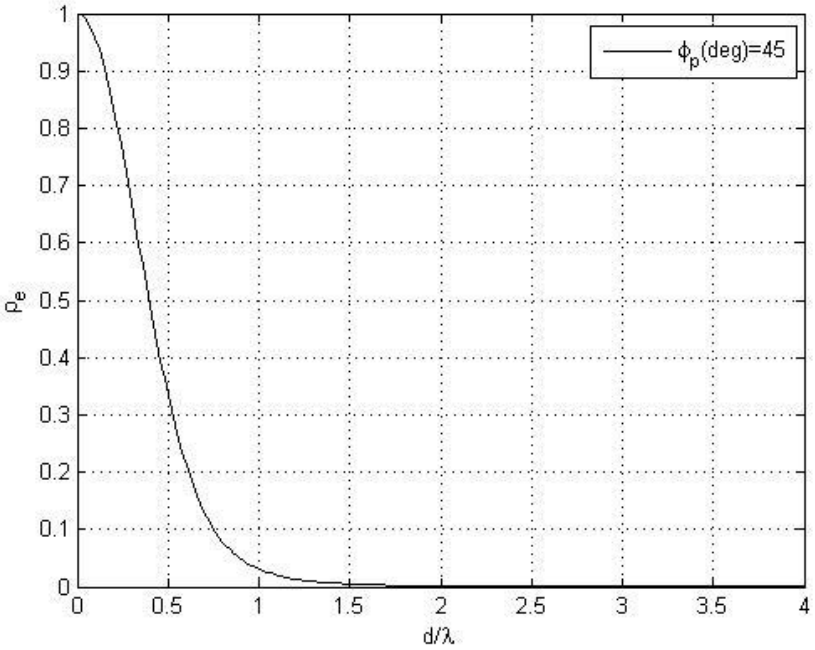

(c) ($\kappa = 4.0$)

Figure 4. Correlations for the case $\phi_p = 45^0$

4.3. case ($\phi_p = 90^0$)

1) isotropic sources

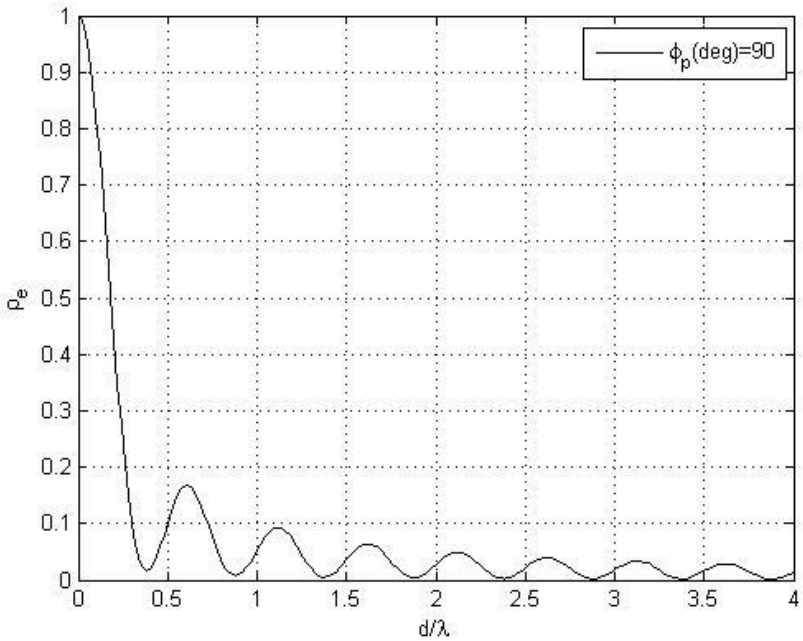

(a) ($\kappa = 0.25$)

2) broadside dipoles

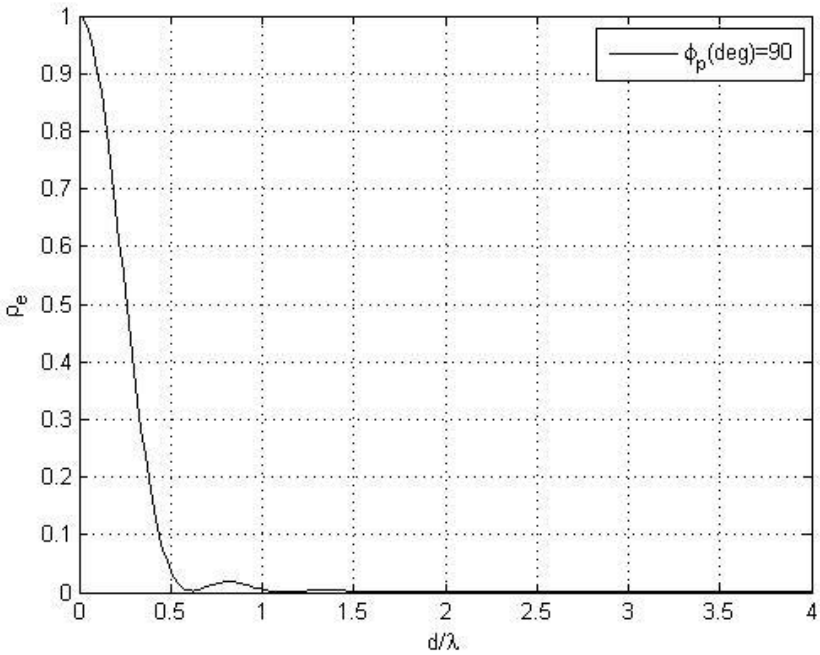

(a) ($\kappa = 0.25$)

1) isotropic sources

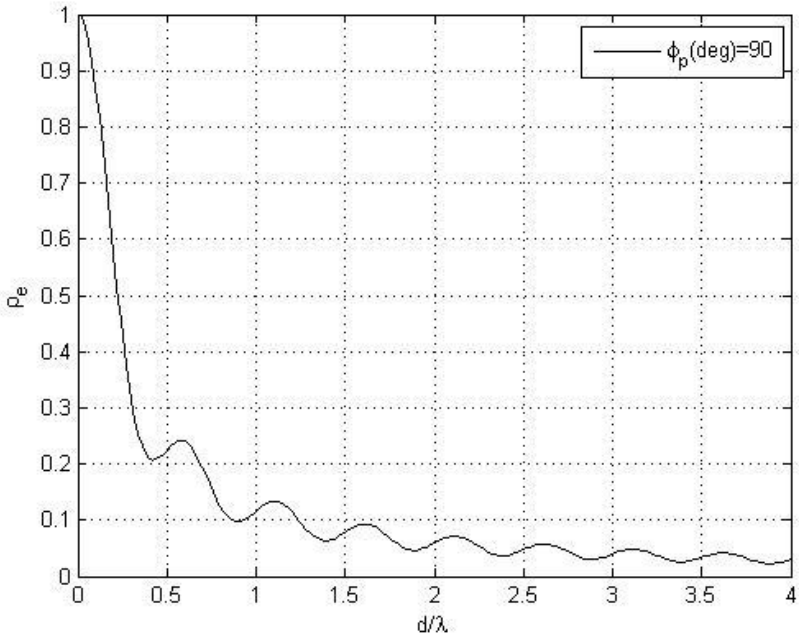

(b) ($\kappa = 1.0$)

2) broadside dipoles

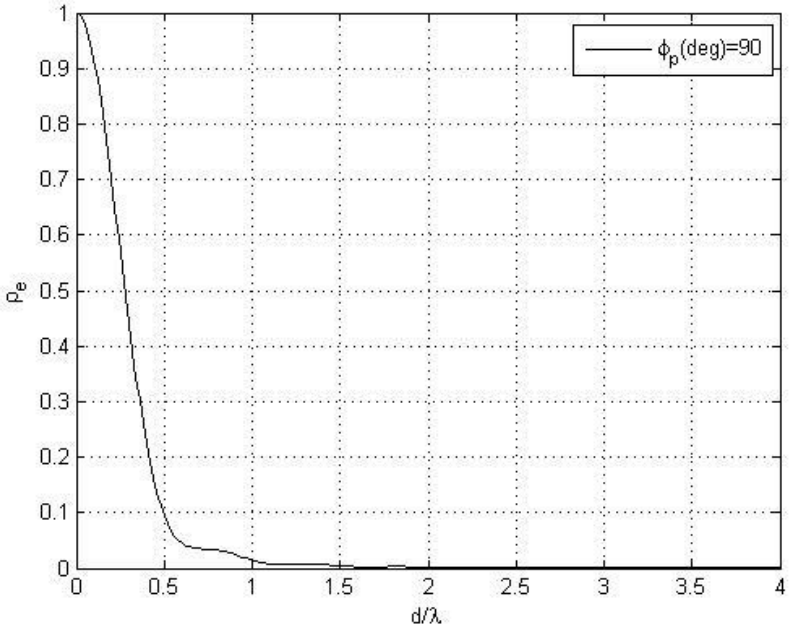

(b) ($\kappa = 1.0$)

1) isotropic sources

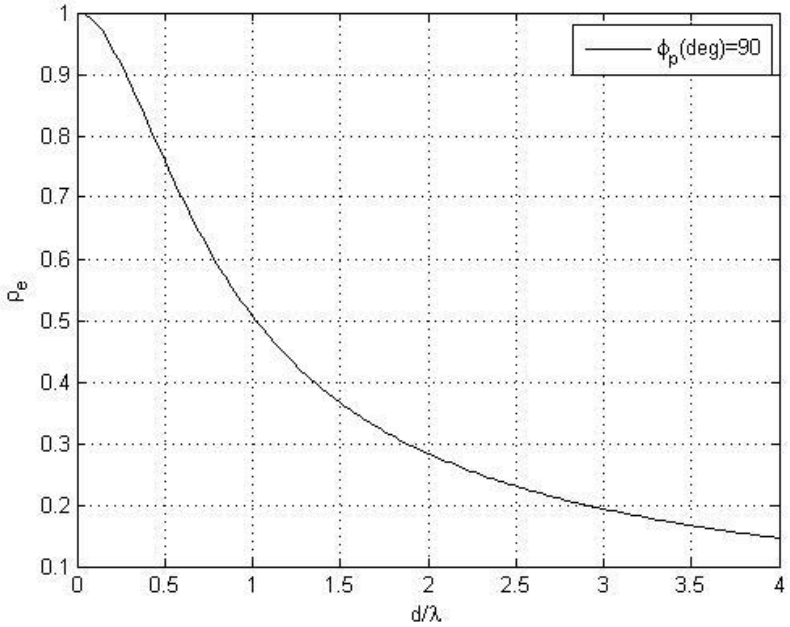

(c) ($\kappa = 4.0$)

2) broadside dipoles

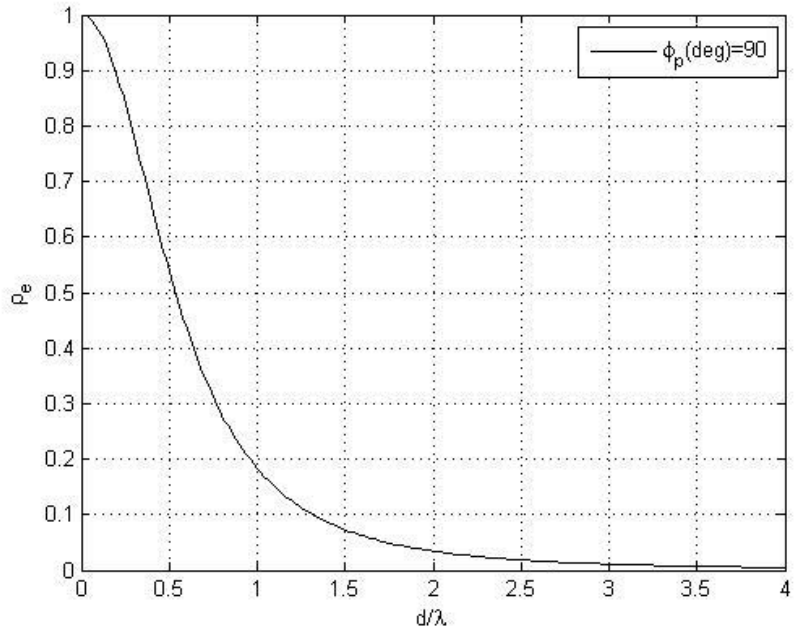

(c) ($\kappa = 4.0$)

Figure 5. Correlations for the case $\phi_p = 90^0$

5. ANALYSIS AND DISCUSSION

Let's now try to physically explain the obtained numerical results for the main lobe of the correlation functions shown in Figs. 3-5. Looking at the main lobe for small von Mises parameter kappa ($\kappa = 0.25$) we see that the correlation is almost independent of the mean AoA (Figs. 3.a.1, 4.a.1, 5.a.1 and Figs.3.a.2, 4.a.2, 5.a.2). That is because for small kappa the AoA distribution is almost uniform and therefore the array illumination only slightly differs for different mean AoA- values.

Generally, the correlation increases with increasing mean AoA (for instance Figs. 3.c.1, 4.c.1, 5.c.1). That can be explained by a decreasing effective (projected) element spacing with increasing mean AoA. For broadside array illumination (mean AoA = 0 degrees) the spatial filtering of the eight shaped radiation pattern of the broadside dipole reduces the effective AoA – spread, leading to a larger correlation in case of the dipole array in comparison with the array of isotropic radiators. This expectation based on physical reasoning agrees with the predictions by our new closed-form expressions (for instance Figs. 3.a.1, 3.a.2). For end-fire array illumination (mean AoA = 90 degrees) and small AoA-spread ($\kappa = 4$) the null in the dipole radiation pattern broadens the effective AoA-distribution (smaller effective AoA-spread) and therefore decreases the spatial correlation. Also this expectation is confirmed by the new spatial correlation model presented in this paper (Figs.5.c.1, 5.c.2).

Looking at the sidelobes of the envelope correlation functions (Figs. 3-5) it can be concluded that these are lowest for the dipole antenna configuration for all considered AoA distributions.

It should be noticed that mutual coupling between antenna elements is not included in the present compact analytical expressions. Depending on the antenna type and the distance

between the array elements an extension of the expressions might be needed. This is the subject of ongoing research.

APPENDIX A

Here the *equivalence* of both models will be proved (our and the model presented in [16]). The key point is the so-called "*Addition theorem*" for Bessel functions [18]

$$Z_\nu(mR) = \sum_{q=-\infty}^{\infty} Z_{\nu+q}(mr) J_q(m\rho) e^{jl\alpha} \tag{A.1}$$

with $Z_\nu(\gamma) = J_\nu(\gamma)$ is arbitrary cylindrical function. Let us set: ν = 0, m = 1. Then, from equation (A.1) we obtain the following formula

$$J_0(R) = \sum_{q=-\infty}^{\infty} J_q(r) J_q(\rho) e^{jl\alpha} \tag{A.2}$$

where

$$R = \sqrt{r^2 + \rho^2 - 2r\rho\cos\alpha} \tag{A.3}$$

Now let us consider the special case

$$r = j\kappa;\ \rho = \frac{2\pi d}{\lambda};\ \alpha = \phi_p - \frac{\pi}{2} \tag{A.4}$$

It can be shown that

$$R = jS \tag{A.5}$$

with S given by (7)

$$S(\xi) = \sqrt{\kappa^2 - \xi^2 + j2\kappa\xi\sin\phi_p} \tag{A.6}$$

This is the argument of our single Bessel function. Next the following property is used

$$J_0(jS) = I_0(S) \tag{A.7}$$

This is the relation between the normal and the modified Bessel function of the first kind and zero order. After division with the modified Bessel function $I_0(\kappa)$ (normalization) we obtain *our expression of the spatial correlation function*

$$\rho_\kappa^{\phi_p}(\xi) = \frac{I_0(S(\xi))}{I_0(\kappa)} \tag{A.8}$$

This equation is the same as our equation (9).

By substituting the parameters from (A.4) into the series expansion (A.2) and using the symmetry

$$J_q(j\kappa) = j^q I_q(\kappa) \tag{A.9}$$

and the equality

$$e^{jq(\phi_p - \pi/2)} = j^{-q} e^{jq\phi_p} \tag{A.10}$$

we come to the following double infinite series expression for the spatial correlation function

$$\rho(d/\lambda) = \frac{1}{I_0(\kappa)} \sum_{q=-\infty}^{\infty} I_q(\kappa) J_q(2\pi d/\lambda) e^{jq\phi_p} \tag{A.11}$$

or

$$\rho(d/\lambda) = \frac{1}{I_0(\kappa)} \sum_{q=-\infty}^{\infty} I_q(\kappa) J_q(2\pi d/\lambda) \left[\cos(q\phi_p) + j\sin(q\phi_p)\right] \tag{A.12}$$

It can be shown that in the *real part* of this series only *even terms* will survive with (cos) functions of order (q = 2n), while in the *imaginary part* of the series only *odd terms* will survive with (sin) functions of order (q = 2n + 1). Here the double infinite series ($-\infty < q < \infty$) can be split into two single infinite series (with positive indices): 1) term with (q = 0); 2) $2\sum_{q=1}^{\infty}(\bullet)$

By taking all these considerations into account the following *equivalent form* of the spatial correlation function can be obtained

$$\begin{aligned}\rho(d/\lambda) = J_0(2\pi d/\lambda) + \frac{2}{I_0(\kappa)} \sum_{n=1}^{\infty} I_{2n}(\kappa) J_{2n}(2\pi d/\lambda) \cos(2n\phi_p) + \\ + j\frac{2}{I_0(\kappa)} \sum_{n=0}^{\infty} I_{2n+1}(\kappa) J_{2n+1}(2\pi d/\lambda) \sin((2n+1)\phi_p)\end{aligned} \tag{A.13}$$

which was derived in [16] for the spatial correlation function (in the case of adjacent isotropic elements in a linear array).

This derivation *proves the equivalence* of our simple closed-form result (9) with the more complicated Bessel-trigonometric series expression from [16] (A.13).

REFERENCES

[1] Y.L.C. de Jong, and M.H.A.J. Herben, "A Tree scattering model for improved propagation prediction in urban microcells", *IEEE Transactions on Vehicular Techn.*, Vol. 53, pp. 503-513, March 2004.

[2] Y.L.C. de Jong, M.H.J.L. Koelen, and M.H.A.J. Herben, "A building transmission model for improved propagation prediction in urban environments", *IEEE Transactions on Vehicular Techn.*, Vol. 53, pp. 490-502, Mar. 2004.

[3] S.V. Savov, and M.H.A.J. Herben, "Modal transmission-line modeling of propagation of plane radiowaves through multi-layer periodic building structures", *IEEE Transactions on Antennas and Propagat.*, Vol. 51, pp. 2244-2251, Sep. 2003.

[4] M.R.J.A.E. Kwakkernaat, Y.L.C. de Jong, R.J.C. Bultitude, and M.H.A.J. Herben, "High-resolution angle-of-arrival measurement on physically-nonstationary mobile radio channels", *IEEE Transactions on Antennas and Propag.*, Vol. 56, pp. 2720-2729, Aug. 2008.

[5] G. J. Foschini and M. J. Gans, "On limits of wireless communications in a fading environment when using multiple antennas", *Wireless Personal Communications*, vol. 6, no. 3, pp. 311–335, 1998.

[6] R. G. Vaughan and J. B. Andersen, *Channels, Propagation and Antennas for Mobile Communications, Volume 2*, Third Edition, Oxford: Clarendon, 2003, pp. 68-73.

[7] L. Chan and S. Loyka, "Impact of multipath angular distribution on performance of MIMO systems", in *Canadian Conf. on Electrical and Computer Engineering*, vol. 2, pp. 853–857, May 2004.

[8] R. G. Vaughan and J. B. Andersen, "Antenna Diversity in Mobile Communications," *IEEE Transactions on Vehicular Techn.*, vol. 36, pp. 149-172, 1987.

[9] P.-S. Kildal, K. Rosengren, "Correlation and Capacity of MIMO Systems and Mutual Coupling, Radiation Efficiency, and Diversity Gain of Their Antennas: Simulations and Measurements in a Reverbation Chamber", *IEEE Communications Magazine*, vol. 39, pp. 104 – 112, Dec. 2004.

[10] K. Rosengren, P.-S. Kildal, "Radiation Efficiency, Correlation, Diversity Gain and Capacity of a six-monopole array Antenna Array for a MIMO System: Theory, Simulation and Measurement in Reverberation Chamber", *IEE Proc. Antennas Propag.*, vol. 152, no. 1, pp. 7 – 16, (+Erratum), Feb. 2005.

[11] I. B. Bonev and S. Savov, "Broadband Investigation of the Spatial Correlation for Antennas for Mobile Phones", *URSI General Assembly*, Istanbul, pp. 7 – 16, Aug. 2011.

[12] S. Blanch, J. Romeu and I. Corbella, "Exact Representation of Antenna System Diversity Performance from Input Parameter Desctription," *IET Electronic Letters*, vol. 39, pp. 705-707, May 2003.

[13] P. Hallboerner, "The Significance of Radiation Efficiencies When Using S-parameters to Calculate the Received Signal Correlation from Two Antennas", *IEEE Antennas Wireless Propag. Letters*, vol. 4, pp. 97 – 99, 2005.

[14] R.H. Clarke, "A statistical theory of mobile radio reception", *Bell System Technical Journal*, Vol. 47, pp. 957-1000, July 1968.

[15] W.C. Jakes, *Microwave Mobile Communications*, IEEE Press, 1974, p. 64.

[16] W.J.L. Queiroz, et. al, ,"Spatial Correlation for DOA Characterization Using Von Mises, Cosine, and Gaussian Distributions", *Intern. Journal on Antennas & Propag.*,Hindawi, no. 540275, pp. 1 – 13, 2011.

[17] M. Abramowitz, I. Stegun, *Handbook of Special Functions*, Dover, New York, 1968, p. 373.

[18] I. Gradshteyn, I. Ryzhik, *Tables of Integrals, Summ, Series and Products*, Nauka, Moscow (in Russian), 1971, p. 417.

INFORMATION SYSTEM FOR MONITORING OF MAGNETIC INDUCTION IN MAGNETOTHERAPY

D. Dimitrov, V. Nikolov

Department of Radiocommunication , Technical University of Sofia,
8 "KlimentOhridski" str., 1000 Sofia , Bulgaria
dcd@tu-sofia.bg

Abstract

The magneto-therapy is very often used actual method in medicine. It's important to be provided permanent monitoring of values of magnetic induction in every point around the human body and in the human body during the procedure of therapy. If one visualization of space distribution of values of magnetic induction in the patient's area would be available on line for the physician, he would be able to do optimization of process of therapy. One new system for magneto-therapy is "magnetic bed", which can provide therapy of every part of the human body separately. This system includes apparatus for magneto-therapy connected with many inductors around the human body. The system can provide "running" low frequency magnetic field using microprocessor unit in the apparatus for magneto-therapy. Special sensors situated in different points of the patient's area provided permanent information about the value of magnetic induction in these points. A microprocessor unit manages on line the process of measurement of magnetic induction in all points in patient's area and providing of computer image of space distribution of value of magnetic induction in the patient's area.

1. INTRODUCTION

In medicine there is often application of low frequency magnetic field in the cases of different diseases. The magnetic field can be used easy not only separately, but together with different medicaments, mineral water, ultrasound etc., also. This is a big advantage of magneto-therapy. According to the medical conclusions the final effect of magneto-therapy can be increased if some or all parameters of magnetic field would be variable [1, 5, 6, 7, 8]. One engineering decision of system for magneto-therapy with variable parameters can be a system with running low frequency magnetic field. These systems are new generation in magneto-therapy. Because of space movement of magnetic field it's possible to be decreased the number of procedures for therapy and to be obtained more easy good effect of therapy. There is not information about devices for permanent monitoring of amplitude of low frequency magnetic induction in the process of therapy [6, 7, 8]. There are some mathematical and computer methods for virtual measurement of amplitude of low frequency magnetic field in magneto-therapy [2, 3, 4].

2. DESIGN OF INFORMATION SYSTEM FOR MONITORING OF PROCESS FOR MAGNETOTHERAPY WITH RUNNING MAGNETIC FIELD

The functional scheme of system for monitoring of magnetic induction in system for magneto-therapy with running magnetic field can be seen in Fig.1. It consists of two basic units : patient's bed for magneto-therapy and unit for measuring of parameters of low frequency magnetic field. The patient's bed consists apparatus for magneto-therapy and inductors. The unit for measuring of parameters of low frequency magnetic field consists magnetic sensors for measurement of magnetic induction of low frequency magnetic field, microprocessor for management of process of measurement of magnetic induction in different point around the human body USB unit and display or PC for visualization of results of measurement . There is feedback from unit for measurement to the apparatus for magneto-therapy for keeping the preliminary defined values of parameters of magnetic induction in different points around the human body and their changes in the time.

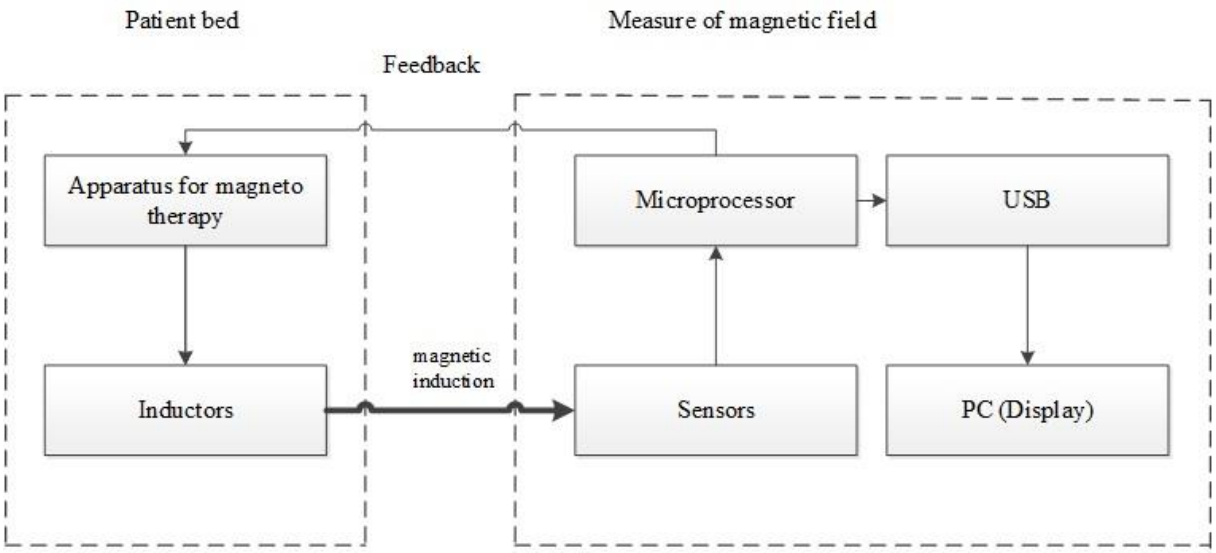

Figure 1. Functional scheme of system for monitoring of magnetic induction in system for magneto-therapy with running magnetic field

The magnetic bed with running low frequency magnetic field can be seen on fig.2. It's consists plastic patient's bed and plastic carriage on the bed, inductors , which are situated on the patient's bed and on the carriage, apparatus for magneto-therapy (under the bed) , sensors for measurement of magnetic induction on every inductor. The apparatus for magneto-therapy provides low frequency pulses of electrical current with preliminary defined parameters according to the program for procedure of therapy. The magnetic inductors are connected to the outputs of apparatus for magneto-therapy. The magnetic sensors are connected to the inputs of microprocessor's unit using coaxial cables for reducing influence of noise. The carriage can do axial movement on the axis of patient's bed during the procedure of therapy or can be without movement according to the medical requirements for therapy. The running of magnetic field can be provided not only on axis of magnetic bed by movement of carriage, but by switchingover of inductors, also. This switching can be according to

different programs of microprocessor's unit. It's clear that it's possible to be provided many kinds of movement (running) of low frequency magnetic field by using microprocessor's unit. This is one of the important advantages of described systems. In the same time can be provided permanent measurement of magnetic induction of magnetic field created by every inductor. On the base of results of these measurements can be provided visualization of space configuration of magnetic field around the human body on the display. The treatment of results of measurements is according of special algorithm, described below. The results of measurement are used simultaneously for feedback from microprocessor's unit to the apparatus for magneto-therapy. There are 8 inductors on the patient's bed and 8 inductors on the carriage (Fig.2). The number of used sensors is 16.

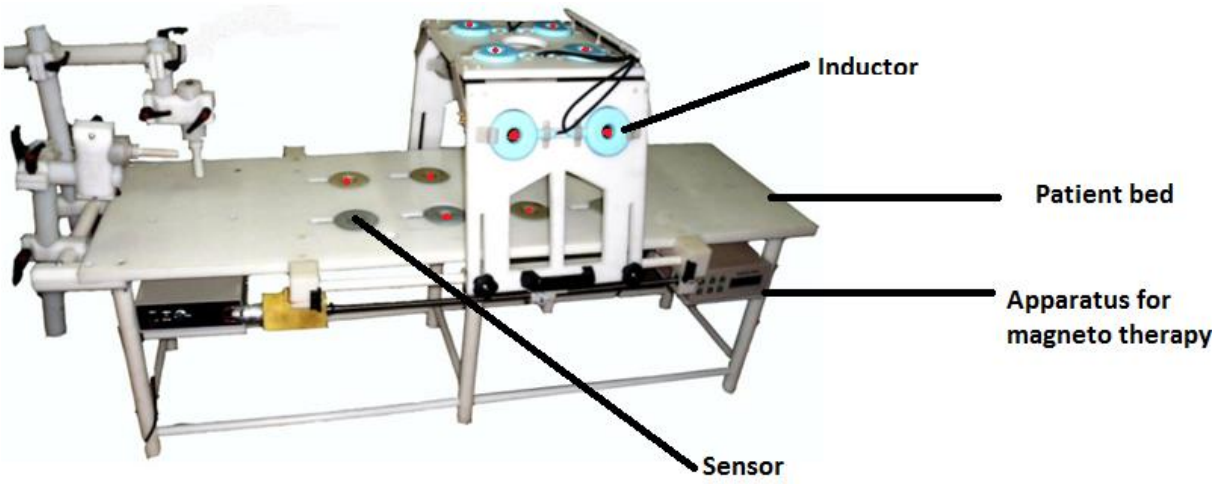

Figure 2. Magnetic bed

3. DESIGN OF MICROPROCESSOR UNIT FOR MANAGEMENT OF MEASUREMENT OF MAGNETIC INDUCTION IN THE PATIENT'S AREA

The scheme of microprocessor's unit can be seen on fig.3. This unit provides :

-conversion of input analog signals from all sensors in to digital signals

-calculation of the maximum measured value of magnetic induction from every sensor using a specific algorithm. This algorithm can be used in the process of measurement of values of magnetic induction in 16 points. The algorithm can be seen below, in Fig.5.

- transfer of measured data to the PC(Display) using USB port (Fig.1) for visualization of space distribution of the values of magnetic induction in patient's area.

-feed back signals to the apparatus for magnetotherapy for keeping preliminary determined parameters of current's pulses in the inductors of magnetic bed (Fig.1).

A microprocessor AT mega 2560 is used for designing of the microprocessor’s unit. This processor is appropriate for management of experimental measurements. The main parameters of microprocessor AT mega 2560 can be seen below:

High Performance, Low Power

High Endurance Non-volatile Memory Segments
–256 KBytes of In-System Self-Programmable Flash
– 4 Kbytes EEPROM
– 8Kbytes Internal SRAM
– Write/Erase Cycles: 10,000 Flash/100,000 EEPROM
– Data retention: 20 yearsat 85°C/ 100 yearsat 25°
Peripheral Features
– Two 8-bit Timer/Counters with Separate Prescaler and Compare Mode
– Four 16-bit Timer/Counter with Separate Prescaler, Compare- and Capture Mode
– Real Time Counter with Separate Oscillator
– Four 8-bit PWM Channels
–Twelve PWM Channels with Programmable Resolution from 2 to 16 Bits
– Output Compare Modulator
–16-channel, 10-bit ADC
–Four Programmable Serial USART
– Master/Slave SPI Serial Interface
– Byte Oriented 2-wire Serial Interface
– Programmable Watchdog Timer with Separate On-chip Oscillator
– On-chip Analog Comparator
– Interruptand Wake-upon Pin Change
Speed Grade: 0 - 16MHz @ 4.5V - 5.5V

Pin Descriptions

Port A (PA7..PA0)

Port A is an 8-bit bi-directional I/O port with internal pull-upresistors (selected for each bit). The Port A output buffer shave symmetrical drive characteristics with both high sinkand source capability. A sinputs, Port A pins thatare externally pulle dlowwill source current if the pull-up resistors are activated. The Port A pin saretri-stated when are set condition become sactive, even if the clock is no trunning.

Port B (PB7..PB0)

Port B isan 8-bit bi-directional I/O port with internal pull-up resistors (selected for each bit). The Port B output buffers have symmetrical drive characteristics with both high sinkand source capability. Asinputs, Port B pin. The Port B pins are tri-stated when are set condition becom es active, even if the clock is not running.

Port C (PC7..PC0)

Port C is an 8-bit bi-directional I/O port with internal pull-up resistors (selected for each bit). ThePort C output buffer shave symmetrical drive characteristics with both high sinkand source capability. A sinputs, Port C pin. The Port C pins are tri-stated when are set condition becom es active, even if the clock is not running.

Used microprocessor in corporates analog-digital converter. The inputs of converter are from ACD0 to ACD15.Depending on the function of the output of the ADC(input or output) in a registeris indicated bylog.0 orl og.1. For the measurement of the magnetic field 16 pcs. sensors are used. Each sensor is connected with a shielded cable to the inputs of built-in ADC with pins from ADC 0 to ADC 15 microprocessor

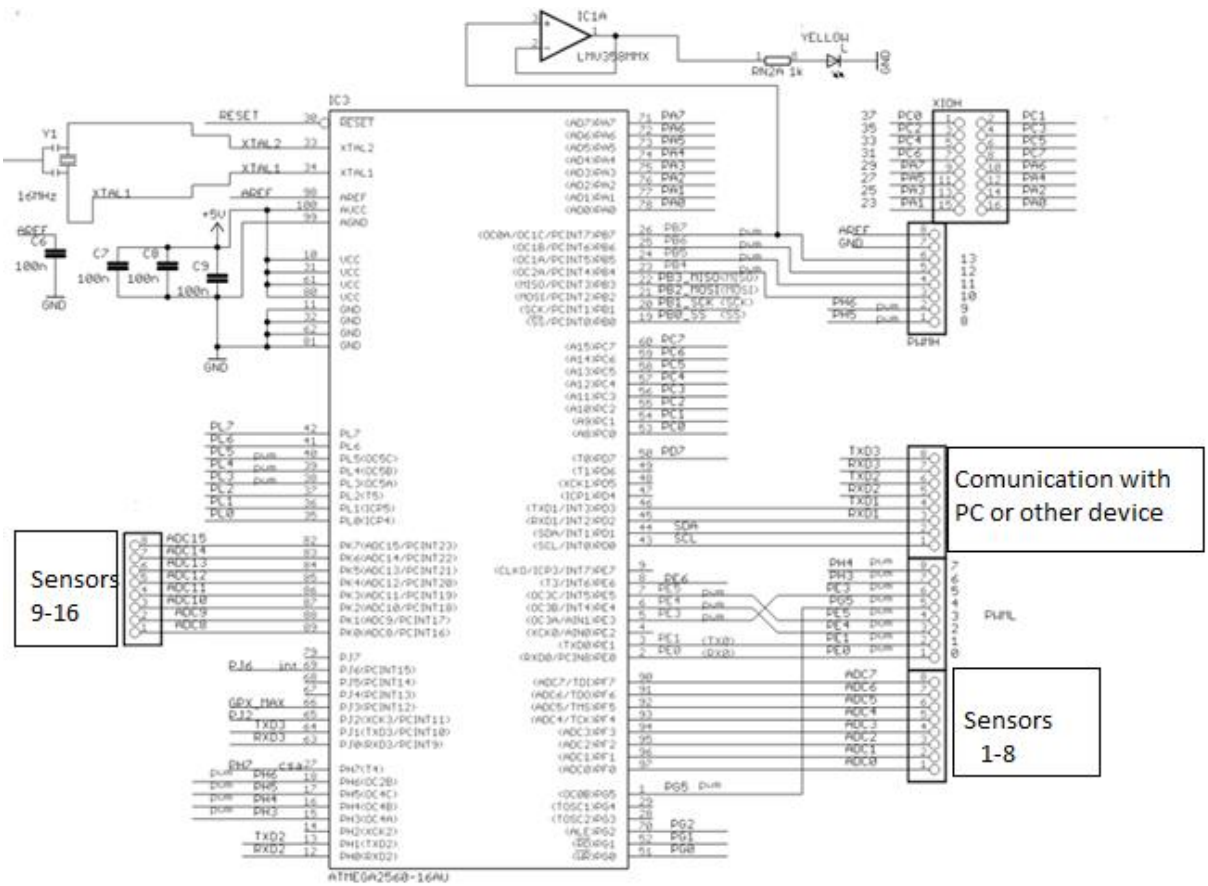

Figure 3. Scheme of microprocessor unit

The sensorsare divided into two groups of 8 units. Sensor1 to 8 and the sensor 9 to16. They are connected to the inputs ofthe integrated circuit. An important conditionfor the proper measurement of values of magnetic inductionis the location of the magnetic sensors.The space disposition of sensors can be seen on fig.2. The values of magnetic induction in the points between sensors can be obtained using interpolation. The microprocessor is powered with DC voltage5 Power of the device can be accomplished in two ways: using an external power supply or by using the built-inUSB plug that connects to a computer or other machinerunning with the USB standard. On Fig.3 can be seen the communication between the microprocessor and external devices. It is performed by the microprocessor using the

following outputs: TX, RX, SCL and SDA Pins.In order toproperly calibrate the ADC ,pin AREF is supplied with a voltagein the range of0 to5V.When properly chosen voltage, the digital values generated by the ADC range from 0 to1023. The maximum measured value of the magnetic field corresponds to 1024. The measured values of magnetic induction are stored in 256K Bytes of-System Self-Programmable Flash. PC is connected to the microprocessor by scheme ATMEGA8U2 (Fig. 4).

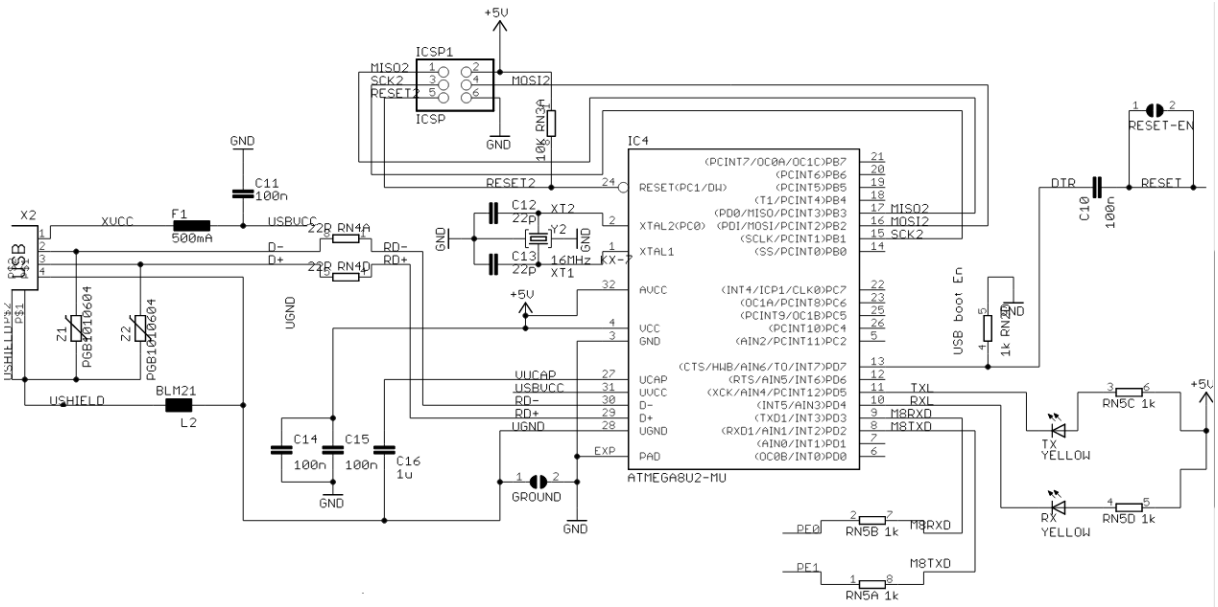

Figure 4. Scheme for connection between microprocessor and PC

4. ALGORITHM FOR MANAGEMENT OF MICROPROCESSOR UNIT IN THE PROCESS OF MEASUREMENT OF MAGNETIC INDUCTION

4.1. Basic principles in the process of measurements

The duration of measurements is 1s.The maximal measured value for this periodis defined as a maximumis recorded in the register as the maximum value.There are also additional control swhich reduces the likel ihood of errors caused by external disturbances. When the measured valueof the amplitude is more high than the preliminary defined maximum possible value of the field, the measured valueis ignored and not included the min determining the maximum value of the measuring field.When the difference between two measured values is more high than a predetermined value, the measured valueis ignored and not included in subsequent measurements in the determination of the maximum valueof the field. In both cases the measurement errors can arise when there is an external disturbance in the system. Because of these preliminary defined requirements the mistakes in the process of measurements can be reduced. The algorithm for management of microprocessor’s unit in the process of measurement of magnetic induction can be seen on fig.5.

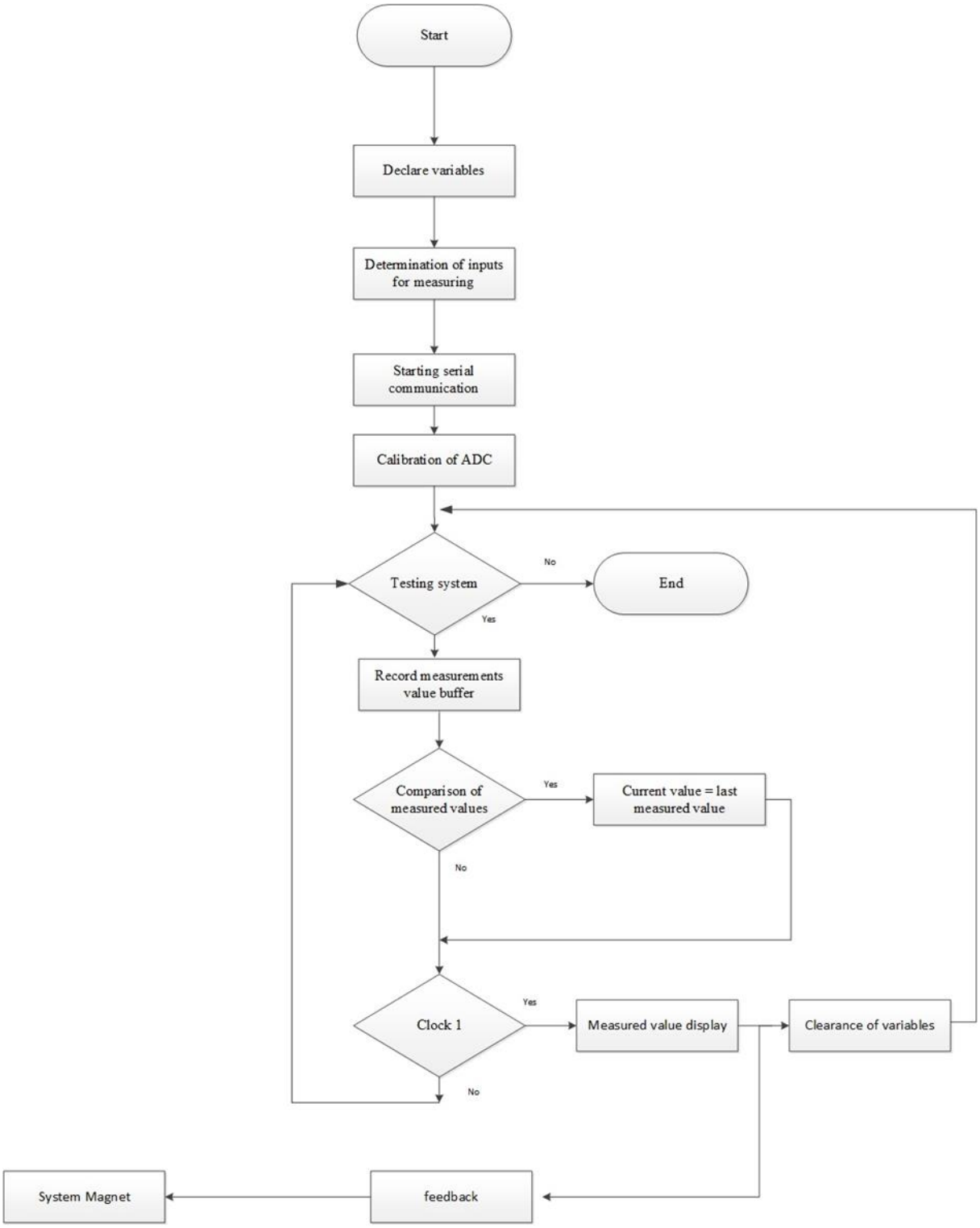

Figure 5. Algorithm for management of microprocessor's unit in the process of measurement of magnetic induction

4.2. Description of algorithm

Declaring variables: This block describes all variables which will be usedin the program of the microprocessor.

Determination of inputs for measurement: In this block,the algorithm determines which pins on the microprocessor will be used, which are input pins and which are output pins. Additionally in this block pins for analog signals and pins for digital signals are defined.

Starting serial communication: This is the block of connection between the microprocessor and the next device (PC), which will be processed measured datais performed via the serial interface.This iteration configures the speed of data transmission between microprocessor and PC.

Calibration of the ADC-This is the block for definition of maximum value of magnetic induction which will be measured using ADC.

Testing of system-This is the cycle in which the program runs continuously.

Recording of measured values from sensors in buffer: In this block the measured values of magnetic induction in every moment are saved in the local memory of microprocessor.

Comparison of measured values: In this block there is a comparison between the value of the instantaneous measured value of the sensor and the previous measured value. If the new measured value is more high than the previous value and the new measured value is more high than the maximum permissible value, the measured value will be determined as maximum and will be stored in the microprocessor. If the above condition is not met, the measured value is ignored.

Clock – 1: In this block should be determinedlength ofthe interval for measurementsof the amplitudeof the magnetic induction(e.g. 1s) and should be choosen the maximummeasured valueofmagnetic induction, whichwill be transmitted to thenext device.

5. CONCLUSION

The described system for monitoring of magnetic induction is very actual and friendly used in magneto-therapy. It's provides on line visualization of space distribution of values of magnetic induction around the human body and in the human body during the procedure of therapy. The microprocessor's unit of this system allows to manage measurement of amplitude of magnetic induction in the case of application of magnetic signals with frequency and/or amplitude modulation. This system allows also to be provided space visualization of space distribution of the values of magnetic induction in the case of "running" low frequency magnetic field. The scheme of described information system, which is suggested in the paper and suggested microprocessor's algorithms for management of simultaneously measurement of the values of magnetic induction in different points are tested successfully in real conditions in hospitals.

REFERENCES

[1] W.Y. Riadh, "Electromagnetic Fields and Radiation (Human Bioeffects and Safety)", Marcel Dekker Inc., Canada, 2001 ISBN 0-8247-0877-3, p.420.

[2] B. Kudrin, V.Nikolov, "Algorithms of interpolation and visualization of low frequency magnetic field by using experimental data" 9th International Conference CEMA'14, Sofia, 2014, pp.43-45.

[3] B. Kudrin, V.Nikolov, "On the mathematical model of interpolation of low frequency Magnetic field using experimental data" 9th International Conference CEMA'14, Sofia, 2014, pp.80-84.

[4] Dimitrov, D. Tz.Dimitrov, A.Computer Simulation of Low Frequency Magnetic Field, Proceedings of 17th EAEEIE Annual Conference on Innovation in Education for Electronical and Information Engineering, Craiova, Romania, 2006, p. 33-36.

[5] Lin, J. C., (ed.), Electromagnetics in Biology and Medicine, Review of Radio Science, 2000, p.330.

[6] Lin, J. C., (ed.), Electromagnetics in Biology and Medicine, Review of Radio Science 1993-1996, Oxford UniversityPress, London, UK, p.470,1996.

[7] Malmivuo, J., and R. Plonsey, Principlesand Applications of Bioelectric and Biomagnetic Fields, Oxford University Press, New York, NY, 1995, p.480.

[8] P. J. Rosch, M. S. Markov, "Bioelectric Medicine", The American Institute of Stress, Yonkers, New York, U.S.A., and New York Medical College, Valhalla, New York, U.S.A.1999, ISBN: 0-8247-4700-3, 1999, p.360.